

Mechanisms of mass transfer to small spheres sinking in turbulence

John M. Lawson^{1,†} and Bharathram Ganapathisubramani¹

¹Department of Aeronautics and Astronautics, University of Southampton, Southampton SO17 1BJ, UK

(Received 20 July 2022; revised 23 November 2022; accepted 24 November 2022)

Using laboratory experiments and numerical simulations, we examine the transfer of soluble material from small, spherical particles sinking in homogeneous turbulence at large Péclet number. A theoretical analysis predicts two distinct mechanisms of convective mass transfer: strain due to turbulence and slip due to gravitational settling. Their relative strength is parametrised by the sinking ratio, $Sr = w_0\tau_\eta/a$, where w_0 is the quiescent settling velocity, a is the particle radius and τ_η is the Kolmogorov time scale. This analysis predicts that the topology of the concentration wake changes from a symmetric topology at $Sr \ll 1$ to an asymmetric topology at $Sr \gg 1$ as the dominant mechanism of mass transfer changes. Particle tracking flow visualisations of small spheres releasing dye in turbulence confirm the existence of this change in mechanism at $Sr = O(1)$. We complement these experiments with numerical simulations of the mass transfer from sinking particles. The transfer rate predicted by the simulation is found to be in good agreement with literature data for mass transfer to turbulent suspensions of solid particles and is consistent with asymptotic expressions for mass transfer in uniform flow when $Sr \gg 1$. A decomposition of the convective fluxes confirms the transition in the transfer mechanism. At $Sr = O(1)$, both mechanisms provide comparable contributions to the transfer rate. Cross-correlation analysis reveals that particle-scale knowledge of both the recent strain and velocity history is required to predict the instantaneous transfer rate. Turbulence-induced particle rotation has a modest suppression effect upon convective transfer by sinking.

Key words: coupled diffusion and flow, particle/fluid flow, homogeneous turbulence

1. Introduction

When small, rigid particles are immersed in a turbulent fluid, diffusible material may be transferred from their surface by convection and diffusion. Often, as is the case for

† Email address for correspondence: j.m.lawson@soton.ac.uk

solutes in liquids, the solute diffuses slowly, so that convection is the dominant mechanism of mass transfer away from the particle. Also, the particle is often small in comparison with the Kolmogorov length scale, the smallest dynamically active scale of the turbulence. This phenomenon occurs in an abundance of engineered and natural processes: chemical products are produced by crystallisation, dissolution, fermentation and heterogeneous reactions in liquid–solid suspensions within stirred tanks and fluidised beds (Myerson 2002; Nienow 2006; Crowe *et al.* 2012); planktonic osmotrophs absorb nutrients (Karp-Boss, Boss & Jumars 1996); pollutants leach from microplastics (Seidensticker *et al.* 2017); bacteria encounter marine viruses (Guasto, Rusconi & Stocker 2012); and breakdown products of marine snow are swept away (Alcolombri *et al.* 2021) as they sink through turbulent ocean waters. In these processes, turbulence, inertia and gravity may drive a convective flow around the particle which enhances mass transfer: gravity may cause particles to sink or float (Harriott 1962), inertia may cause particles to slip (Levins & Glastonbury 1972*b*) and turbulent eddies may convect material away by strain (Batchelor 1980; Lawson & Ganapathisubramani 2021). In this paper we ask: for small spherical particles sinking in a turbulent flow, what is the dominant mechanism of mass transfer?

The relative importance of these mechanisms to convective mass transfer, and in some cases their very existence, has been debated extensively in the context of stirred tank reactors (Pangarkar *et al.* 2002; Pangarkar 2015). As reviewed by Pangarkar *et al.* (2002), the proposed mechanisms of mass transfer to small particles fall under three categories: slip velocity theory, penetration theory and Kolmogorov theory. In the slip velocity theory, first proposed by Calderbank & Moo-Young (1961) and later developed by Harriott (1962), the particle experiences a relative flow due to gravitational settling and its inertial response to turbulent velocity fluctuations. A concentration boundary layer develops whose thickness is controlled by the relative magnitude of diffusion and slip-driven flow and material is swept away from the particle in a single wake. Semi-empirical expressions have subsequently been developed for the particle Sherwood number Sh , a dimensionless measure of the mass transfer rate. These expressions are generally of the form (Nienow 1992)

$$Sh = 1 + \alpha Re_w^\beta Sc^\gamma, \quad (1.1)$$

where $Re_w = wa/\nu$ is the particle Reynolds number based on the (effective) slip velocity w , radius a and kinematic viscosity ν , and $Sc = \nu/D$ is the Schmidt number. The exponents β and γ are sometimes fixed to be 1/2 and 1/3, respectively, in order to be consistent with the expected scaling of the concentration boundary layer from boundary layer theory and empirical observations of mass transfer from steadily falling particles (Frössling 1938; Ranz & Marshall 1952).

For neutrally buoyant particles, Harriott (1962) noted this slip velocity must vanish and that mass transfer must be provided by another mechanism. Harriott (1962) and later Armenante & Kirwan (1989) therefore proposed refinements of penetration theory (Higbie 1935), in which mass transfer from the particle is limited by unsteady diffusion under the action of eddies which periodically replenish the concentration boundary layer with fresh fluid. This predicts a mass transfer rate of similar form to (1.1), but with a Reynolds number $Re_\epsilon = a^{4/3}\epsilon^{1/3}/\nu$ redefined in terms of the energy dissipation rate ϵ . However, the predicted exponents for small spherical particles ($\beta = 3/4$, $\gamma = 1/2$) are at variance with the available experimental data (Armenante & Kirwan 1989). Furthermore, the role of the convective flow due to slip (e.g. by sinking) is not incorporated.

An alternative approach for the near-neutrally-buoyant case is offered by Kolmogorov theory (e.g. Calderbank & Moo-Young 1961; Levins & Glastonbury 1972*a*). In this, an

effective slip velocity is introduced which is taken to grow with the magnitude of inertial range velocity differences $\Delta u \sim (\epsilon a)^{1/3}$, where ϵ is the mean dissipation rate and Δu is the characteristic velocity difference between two points in the flow separated by scale a . This also results in a particle Reynolds number Re_ϵ based on the dissipation rate ϵ for use in (1.1). Whilst the rationale for such a slip velocity is understandable for particles sized in the inertial range, this velocity scale has also been applied to data of particles in the dissipation range, where the rationale is questionable (Armenante & Kirwan 1989). Several other authors (e.g. Levins & Glastonbury 1972*b*; Ohashi, Sugawara & Kikuchi 1981; Armenante & Kirwan 1989) have also formulated an effective slip velocity (on dimensional grounds) based upon the dissipation rate, particle size and viscosity, which is equivalent to the Kolmogorov scaling argument. The specific mechanism of mass transfer is not elucidated in these works and no physical interpretation is given to the effective slip velocity (as emphasised by, for example, Levins & Glastonbury (1972*b*) and Armenante & Kirwan (1989)).

Later, Batchelor (1980) introduced a theory of mass transfer to small, suspended solid spheres. The Reynolds number of the motion in the neighbourhood of the particle, associated with either the slip Re_w or the turbulence Re_ϵ , is assumed to be small compared with unity. This assumption implies that the particle Stokes number $St \sim Re_\epsilon^{3/2} \ll 1$ is also small. This allows the relative flow field to be prescribed as a superposition of a uniform slip velocity, linear velocity gradient and a Stokes perturbation due to the presence of the particle. The concentration boundary layer that develops is analysed with the use of classic asymptotic methods (Leal 2012). Because the flow is turbulent, the components of the linear gradient and slip velocity fluctuate in time. Batchelor then argues that at large turbulent Péclet number $Pe = a^2 \tau_\eta / D = Re_\epsilon^{3/2} Sc$, due to the convection-suppression effect (Batchelor 1979), particle motion due to slip has a negligible effect on the mass transfer rate because the particle rotates isotropically. This convection-suppression mechanism has recently been confirmed in turbulent flows to suppress convective mass transfer by velocity fluctuations occurring on a time scale more rapid than $\tau_\eta Pe^{1/3}$ (Lawson & Ganapathisubramani 2021). In the limit of $Pe \rightarrow \infty$, Batchelor concluded that for small spherical particles, the only component of the relative flow field which is persistent upon averaging over time in the particle reference frame is an axisymmetric strain, whose magnitude scales with $1/\tau_\eta$. In the limit of large turbulent Péclet number, this axisymmetric straining flow drives a mass transfer rate like

$$\begin{aligned} Sh &= 0.55Pe^{1/3} + O(1) \\ &= 0.55Re_\epsilon^{1/2} Sc^{1/3} + O(1). \end{aligned} \tag{1.2}$$

In a reference frame following and rotating with the particle, the solution of concentration boundary layer near the surface asymptotically approaches that of a spherical particle in an axisymmetric extensional strain. This result places empirical correlations based on Kolmogorov theory for small particles on firmer physical grounds, provided that the mechanism of mass transfer due to an effective slip velocity is reinterpreted as mass transfer by the (time-average) ambient straining field.

A striking implication of this analysis is that convection due to slip (e.g. by gravity or inertia) is suppressed at large turbulent Péclet number. Batchelor (1980) remarks that the ‘strange consequence’ for sinking particles is that gentle stirring should initially decrease the average mass transfer rate. Batchelor’s prediction (1.2) shows reasonable agreement with available experimental data for nearly neutrally buoyant spheres, but conflicts with the observed enhancement of mass transfer for particles where a significant density difference exists (Harriott 1962; Levins & Glastonbury 1972*b*). The question therefore arises as to

how to reconcile the mechanisms of slip and strain in a theory of particle-scale mass transfer.

Recently, we have examined Batchelor's scenario numerically for small, neutrally buoyant spheroids in isotropic turbulence at large but finite turbulent Péclet number (Lawson & Ganapathisubramani 2021). The motion of spherical and spheroidal tracer particles is simulated in homogeneous, isotropic turbulence and the relative velocity field, which is prescribed by the Lagrangian time history of the linear velocity gradient and Stokes perturbation sampled by the tracer, is used to force the numerical solution of the convection–diffusion equation in the vicinity of the particle. The mass transfer rate predicted by these simulations is found to be in good quantitative agreement with available experimental data for small, spherical particles in turbulence. The results confirm the convection-suppression effect and demonstrate that the concentration boundary layer is unresponsive to velocity fluctuations occurring on a time scale more rapid than $\tau_d \sim \tau_\eta Pe^{1/3}$. The instantaneous mass transfer rate is shown to correlate most strongly with the relative velocity field filtered on this time scale. The conceptual picture that emerges from this analysis is that the instantaneous concentration field near the particle surface is close to the steady-state solution of an equivalent particle subject to the same (time-filtered) relative velocity field. In this interpretation, it is not necessary for slip to make negligible contribution to the mass transfer rate, because a slip velocity may be persistent over shorter times.

In this paper, we examine the mechanisms of mass transfer to small particles sinking in turbulence. In § 2, we revisit the theoretical description given by Batchelor (1980) of small spheres exchanging material in a turbulent flow and identify that at large but finite turbulent Péclet number, the sinking ratio $Sr = w_0 \tau_\eta / a$ forms an important control parameter of the mass transfer problem. We also examine qualitatively the properties of the scalar wake in the limits of $Sr \ll 1$ and $Sr \gg 1$. In § 3, we present a set of flow visualisation experiments designed to identify the mechanism of mass transfer to hydrodynamically small, spherical particles as the sinking ratio is varied. These measurements allow us to reconstruct the instantaneous concentration field in the vicinity of small particles exchanging material with a turbulent flow. This is achieved by visualising the release of dye from small, spherical ion-exchange beads in homogeneous turbulence using shadowgraphic particle tracking and planar laser-induced fluorescence measurements. We describe our methodology and data reduction in §§ 3.1 and 3.2, respectively, and present particle-scale flow visualisations of mass transfer in § 3.3. Our observations confirm that a change in the mechanism of mass transfer occurs when $Sr = O(1)$. Based on these experimental insights, we present an extension of our numerical model in § 4 to incorporate the effect of gravity for heavy particles and examine the influence upon the mass transfer rate. After providing a validation of the average transfer rate predicted by our simulations in § 4.2, we quantify the mechanisms of mass transfer in §§ 4.3 and 4.4. The results provide insight into reconciling the two mechanisms in particle-scale mass transfer models. We provide a brief discussion and conclusions in § 5.

2. Theoretical background

In this section, we provide an analytical description of the mass transfer from a dilute suspension of sinking particles. This forms the basis of our numerical model in § 4 and formally identifies Sr as a control parameter in the mass transfer problem. Furthermore, we identify qualitative properties of the scalar wake in the limits of $Sr \ll 1$ and $Sr \gg 1$ at large but finite Pe . We base our approach on Batchelor (1980), which describes the relative

flow field near the particle in terms of a fluctuating slip velocity, turbulent shear and Stokes perturbation. The particle Reynolds number is assumed to be small, so that the Stokes flow approximation is valid. Furthermore, gravitational acceleration is assumed to be strong in comparison with the turbulence.

Let us consider the motion of a small spherical particle of radius a with position $\mathbf{X}(t)$ and velocity $\dot{\mathbf{X}}$ in an unsteady turbulent flow field $\mathbf{u}(\mathbf{x}, t)$ under the action of gravitational acceleration $\mathbf{g} = g\mathbf{e}_z$. The spatial coordinate of the laboratory frame is \mathbf{x} and temporal coordinate is t . When the particle Reynolds number is sufficiently small, the forces on the particle are prescribed by Stokes flow, and the equation of motion is given by

$$\ddot{\mathbf{X}} = \frac{1}{\tau_p}(\mathbf{u}(\mathbf{X}, t) - \dot{\mathbf{X}}) + \beta \frac{D\mathbf{u}}{Dt} + (1 - \beta)g\mathbf{e}_z + \text{Basset history and Saffman lift}, \quad (2.1)$$

where $\tau_p \equiv a^2/(3\beta\nu)$ is the response time of the particle and $\beta = 3\rho_f/(2\rho_p + \rho_f)$ is the density ratio parameter, in which ρ_p is the density of the particle and ρ_f is the density of the fluid. The Stokes number $St = \tau_p/\tau_\eta$ is the measure of the particle response time in comparison with the time scale of the turbulence and implicitly defines the particle size in comparison with the Kolmogorov scale as $a/\eta = (3\beta St)^{1/2}$. In the small-particle limit $St \ll 1$, τ_p is a small parameter and, regardless of initial conditions, the slip velocity $\mathbf{w}_0(\mathbf{X}, t) = \mathbf{u}(\mathbf{X}, t) - \dot{\mathbf{X}}$ exponentially relaxes towards (Ferry & Balachandar 2001)

$$\mathbf{w}_0(\mathbf{X}, t) = (1 - \beta) \left(\frac{D\mathbf{u}}{Dt} - \mathbf{g} \right) \tau_p + O(\tau_p^{3/2}). \quad (2.2)$$

Therefore, when the gravitational acceleration is much stronger than the material acceleration due to turbulence (i.e. $D\mathbf{u}/Dt \ll \mathbf{g}$), the slip velocity is

$$\mathbf{w}_0 = (\beta - 1)g\tau_p = w_0\mathbf{e}_z \quad (2.3)$$

to leading order in τ_p . This is simply the settling velocity in quiescent flow and becomes independent of tracer position \mathbf{X} and time t . The fluid acceleration is a small-scale quantity which scales with the Kolmogorov scale $a_\eta = (\epsilon^3/\nu)^{1/4}$ (Voth *et al.* 2002), so (2.3) is valid for small Froude number $Fr = a_\eta/g \ll 1$. This restricts the choice of Sr , St and the density ratio β via the relationship

$$Sr = \frac{|1 - \beta| St^{1/2}}{\sqrt{3\beta} Fr}. \quad (2.4)$$

Thus if we fix St and Fr to be much smaller than unity, the density ratio β essentially controls the sinking ratio. These joint assumptions are restrictive but relevant to our motivating examples. For instance, a quick calculation based on Karp-Boss *et al.* (1996) shows that marine diatoms absorb nutrients in turbulent environments with $St \ll 1$ and $Fr \ll 1$. Similarly, a common design requirement for bioreactors is for cells to be much smaller than the Kolmogorov scale to avoid shear-induced damage (i.e. $St \ll 1$) (Nienow 2006), which typically results in small Froude numbers also.

The relative velocity field in the frame co-moving with the tracer $\mathbf{w}(\mathbf{r}, t) = \mathbf{u}(\mathbf{X} + \mathbf{r}, t) - \dot{\mathbf{X}}$ is given as a superposition of the slip velocity, the ambient linear velocity gradient surrounding the particle plus a perturbation due to the Stokes flow surrounding the particle. This is

$$\mathbf{w}(\mathbf{r}, t) = \mathbf{w}_0 + \mathbf{G}(\mathbf{X}, t)\mathbf{r} + \mathbf{w}'(\mathbf{r}, t), \quad (2.5)$$

where $G_{ij} = \partial u_i/\partial x_j$ is the velocity gradient tensor sampled at the particle position and $\mathbf{w}'(\mathbf{r}, t)$ is the Stokes perturbation due to the presence of the particle. For an infinitesimal

particle, this Stokes perturbation is expressed as a function of the instantaneous slip velocity \mathbf{w}_0 , gradient \mathbf{G} and the boundary condition at the particle surface $|\mathbf{r}| = a$ (Kim & Karrila 1991).

As the particle translates, it is also free to rotate with angular velocity $\boldsymbol{\Omega} = \boldsymbol{\omega}/2$ prescribed by the ambient vorticity $\boldsymbol{\omega}$ (Jeffery 1922). Therefore, in the coordinate system \mathbf{y} co-moving and co-rotating with the particle, we have $\mathbf{r} = \mathbf{R}\mathbf{y}$, where the orientation of the body frame \mathbf{R} evolves as

$$\frac{d\mathbf{R}}{dt} = [\boldsymbol{\Omega}]_{\times} \mathbf{R}. \tag{2.6}$$

The ambient velocity field $\mathbf{v}(\mathbf{y}, t)$ in this co-rotating system is therefore

$$\begin{aligned} \mathbf{v}(\mathbf{y}, t) &= \mathbf{R}^T \mathbf{w} + \dot{\mathbf{R}}^T \mathbf{r}, \\ &= \mathbf{v}_0 + \mathbf{E}\mathbf{y} + \mathbf{v}'(\mathbf{y}, t), \end{aligned} \tag{2.7}$$

where we have introduced $\mathbf{v}_0 = \mathbf{R}^T \mathbf{w}_0$ as the settling velocity in the co-rotating frame, $\mathbf{E} = \mathbf{R}^T (\mathbf{G} - [\boldsymbol{\Omega}]_{\times}) \mathbf{R}$ is the rate-of-strain tensor in this frame and $\mathbf{v}'(\mathbf{y}, t) = \mathbf{R}^T \mathbf{w}'$ is the Stokes perturbation in the rotating frame. We note that in this co-rotating frame, the fluid is at rest at the particle surface $|\mathbf{y}| = a$.

The convection–diffusion equation can now be written in dimensionless form, normalising by the particle radius a and Kolmogorov timescale τ_η (Leal 2012; Lawson & Ganapathisubramani 2021):

$$\frac{\partial \theta}{\partial t^*} + \mathbf{v}^* \cdot \nabla_* \theta = \frac{1}{Pe} \nabla_*^2 \theta, \tag{2.8}$$

where $\theta(\mathbf{y}^*, t)$ is the (dimensionless) concentration of the solute. Our convention is that terms written with a superscript $*$ (e.g. $\mathbf{v}^* = \mathbf{v}\tau_\eta/a$, $\mathbf{y}^* = \mathbf{y}/a$) have been non-dimensionalised with τ_η and a . The turbulent Péclet number is defined as $Pe \equiv a^2/D\tau_\eta$ for solute diffusion coefficient D . We distinguish this from the quiescent settling Péclet number $Pe_w \equiv aw_0/D = PeSr$. We consider a uniform concentration boundary condition:

$$\left. \begin{aligned} \theta(\mathbf{y}^*, t) &= 1 & |\mathbf{y}^*| &= 1 \\ \theta(\mathbf{y}^*, t) &= 0 & |\mathbf{y}^*| &\rightarrow \infty. \end{aligned} \right\} \tag{2.9}$$

This corresponds to a uniform (dimensional) concentration at the particle surface C_1 and uniform concentration far from the particle C_0 with $\theta = (C(\mathbf{y}, t) - C_0)/(C_1 - C_0)$. The Sherwood number, the non-dimensional measure of the solute flux Q , is defined as

$$Sh = \frac{Q}{4\pi r D (C_1 - C_0)} = -\frac{1}{4\pi Pe} \iint_{|\mathbf{y}^*|=1} \nabla_* \theta \cdot d\mathbf{S}. \tag{2.10}$$

Thus, $Sh = 1$ for a sphere with mass transfer by diffusion alone.

Let us examine the magnitude of the terms in the non-dimensionalised relative velocity field:

$$\mathbf{v}^*(\mathbf{y}^*, t^*) = \underbrace{\frac{v_0 \tau_\eta}{r}}_{O(w_0 \tau_\eta/a)} + \underbrace{\mathbf{E}^* \mathbf{y}^*}_{O(y/a)} + \mathbf{v}'^*(\mathbf{y}^*, t^*). \tag{2.11}$$

The slip velocity has magnitude $w_0 \tau_\eta/a$, although its orientation changes with time as the particle rotates. Near the particle, the influence of the linear velocity gradient is $O(1)$,

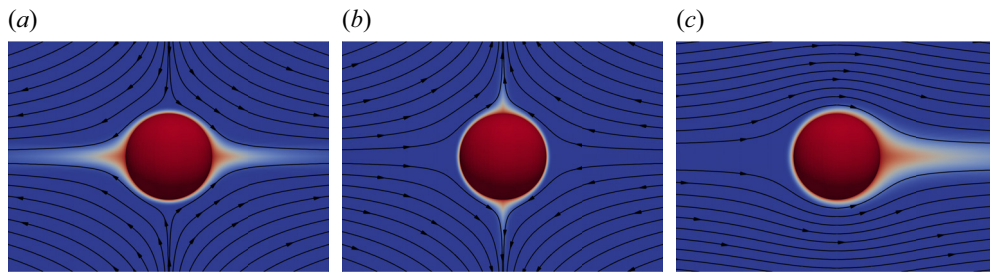


Figure 1. Illustration of solute transfer from a small, spherical particle at large Péclet number under steady (a) extensional axisymmetric strain, (b) compressive axisymmetric strain and (c) uniform flow.

and the Stokes perturbation is comparable to the sum of these terms. The sinking ratio $Sr \equiv w_0 \tau_\eta / a$ therefore forms a natural control parameter of the problem, in addition to the turbulent Péclet number, the Stokes number and density parameter.

Batchelor (1980) argued that in the limit of $Pe \rightarrow \infty$, the solution of (2.8) near the particle surface asymptotically approaches the solution of

$$\tilde{\mathbf{v}}^* \cdot \nabla \theta = \frac{1}{Pe} \nabla^2 \theta, \quad (2.12)$$

where

$$\tilde{\mathbf{v}}^*(\mathbf{y}^*, t^*) = \frac{1}{\tau_f^*} \int_{-\tau_f^*}^0 \mathbf{v}^*(\mathbf{y}^*, t^* + t') dt' \quad (2.13)$$

is the relative velocity field averaged over a long time τ_f^* . This is justified on the basis that the concentration boundary layer becomes insensitive to velocity fluctuations that are more rapid than $\tau_\eta Pe^{1/3}$ due to the convection-suppression effect (Batchelor 1979; Lawson 2021). Taking the average in the limit $\tau_f^* \rightarrow \infty$, Batchelor (1980) concluded that the average convective contribution due to slip in (2.11) vanishes, because the particle orientation is isotropic in the large-time limit. Therefore, in Batchelor's analysis, the sinking ratio does not appear as a control parameter. However, for neutrally buoyant spheroids, we have empirically shown shown that at large but finite Pe , the solution of (2.8) is best approximated by (2.12) when the time scale is chosen $\tau_f^* \sim Pe^{1/3}$ (Lawson & Ganapathisubramani 2021). Under this hypothesis, it is therefore still possible for slip to contribute to the convective mass transfer, because $\tilde{\mathbf{v}}_0^*$ does not vanish when averaging over a finite time interval.

Figures 1(a) and 1(b) illustrate the topology of the concentration field for solute transfer from a spherical particle in steady, axisymmetric strain, i.e. $Sr \ll 1$. Solute is advected away from the particle by convection due to strain in a thin, symmetric, line-like (figure 1a) or sheet-like (figure 1b) wake, depending upon the direction of the strain along the symmetry axis. On the other hand, under uniform slip $Sr \gg 1$ (figure 1c), solute streams from the particle along a single, line-like wake. Therefore, the mechanism of the mass transfer and the topology of the wake are predicted to be qualitatively different at $Sr \ll 1$ and $Sr \gg 1$.

3. Laboratory experiments

In this section, we present a set of flow visualisation experiments designed to identify the mechanism of mass transfer to hydrodynamically small, spherical particles as the

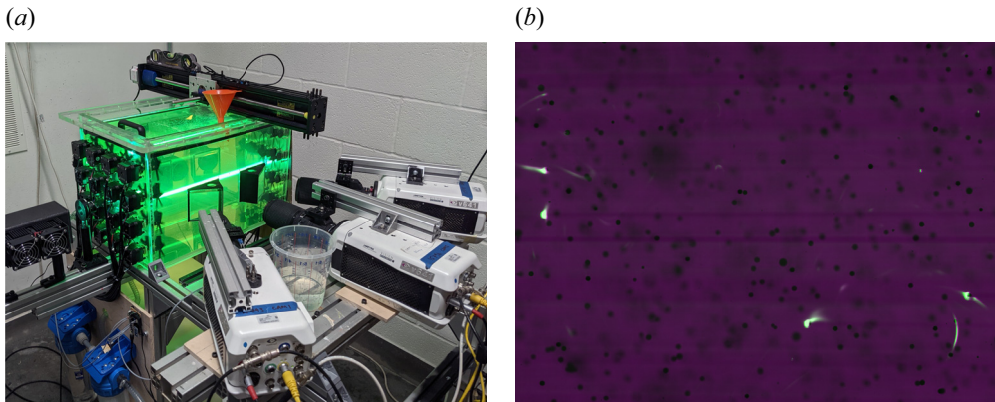


Figure 2. (a) Photograph of experimental apparatus, illustrating: impeller-stirred mixing tank; high-speed shadowgraph imaging arrangement including cameras, prisms and collimated backlight sources; and PLIF laser, optics and sheet. (b) Visualisation of the concentration boundary layer and wake around fine particles in turbulence, showing PLIF image (green channel) and shadowgraph image of particle (purple channel). Supplementary movies 1 and 2 available at <https://doi.org/10.1017/jfm.2022.998> show sample PLIF/shadowgraph video sequences.

sinking ratio is varied. The basic principle is to load spherical ion-exchange beads with a fluorescent anionic dye (fluorescein) which is released upon contact with a sodium chloride solution. We then track the motion of particles in homogeneous turbulence using high-speed shadowgraph imaging and visualise the dye release using planar laser-induced fluorescence (PLIF). Resultant three-dimensional (3-D) reconstructions of the concentration field are then analysed to statistically characterise the concentration wake as a function of the sinking ratio.

3.1. *Experimental methodology*

Here, we describe our experimental set-up and our procedure for tracking particles and reconstruct the concentration field surrounding the particle. Our experimental set-up is illustrated in [figure 2\(a\)](#). It consists of three main components: a randomly stirred mixing tank to generate homogeneous turbulence, dye-laden particles and a combined shadowgraph and PLIF imaging set-up to track particles to obtain particle-scale measurements of dye release. We now describe each.

3.1.1. *Mixing tank*

To generate homogeneous turbulence in our laboratory, we use the randomly stirred mixing tank facility described in Lawson & Ganapathisubramani (2022). We provide a brief description here. It consists of a 45 l capacity transparent poly(methyl methacrylate) (PMMA) tank (internal dimensions 500 mm × 300 mm × 300 mm) with a removable lid and 32 pitched-blade impellers, driven by independently controlled stepper motors. These are spaced 75 mm apart on a 4 × 4 square grid and are mounted through the side-wall of the tank. The lid of the tank is removable; the tank is filled with water to a level slightly above the lid. Between experimental runs, the water was drained and refilled twice to ensure the tank was clean and free of dye. The water temperature was not regulated and varied between $T = 20$ and 21 °C. Based on this temperature measurement, we obtain the

mass density ρ_f , kinematic viscosity ν and dynamic viscosity μ of the water from literature data (Lide 2013).

To create unsteady forcing, we implement the ‘sunbathing’ algorithm of Variano & Cowen (2008), which has been widely used in jet-stirred mixers (Variano & Cowen 2008; Bellani & Variano 2014; Carter *et al.* 2016; Pérez-Alvarado, Mydlarski & Gaskin 2016; Esteban, Shrimpton & Ganapathisubramani 2019). We drive the impellers at a fixed rotation rate f_I whilst randomly reversing the direction of motion. Each impeller switches between spinning clockwise for a time τ_F and then anticlockwise for a time τ_R . Following Variano & Cowen (2008), the durations of forward thrust $\tau_F \sim \mathcal{N}(\mu_F, \mu_F/3)$ and reverse thrust $\tau_R \sim \mathcal{N}(\mu_R, \mu_R/3)$ are drawn from a normal distribution (clipped at zero) with means μ_F, μ_R and standard deviations $\mu_F/3, \mu_R/3$. Following Lawson & Ganapathisubramani (2022), we choose a source fraction $\phi = \mu_F/(\mu_F + \mu_R) = 0.25$ and a forcing period $\mu_F + \mu_R = 32$ s, which are chosen to optimise the intensity and homogeneity of the turbulence.

We have previously characterised the turbulence generated in our mixing tank using particle image velocimetry (PIV) (Lawson & Ganapathisubramani 2022). The mean flow at the centre of the tank is weak, accounting for around 1%–4% of the total kinetic energy in the 75 mm \times 75 mm \times 75 mm region near the geometric centre. Here, the flow is dominated by nearly isotropic turbulent velocity fluctuations, which have a characteristic magnitude u' and are homogeneous to within the standard statistical uncertainty ($\pm 2.2\%$) of our PIV measurements. The mean dissipation rate ϵ at the centre of the tank was obtained from fits of the second-order structure function. Additionally, using the large-eddy PIV method (De Jong *et al.* 2009), we have found the spatial distribution of the mean energy dissipation rate is homogeneous to within $\pm 41\%$ of the spatial average near the centre of the tank. The integral autocorrelation length scale in this region is around 58–70 mm. We conclude that the recent Lagrangian history of the particles observed in our measurement volume approximates that found in homogeneous, isotropic turbulence.

3.1.2. Dye-laden particles

To create spherical dye-laden particles, we load sodium fluorescein dye (Sigma Aldrich) onto commercially available anion-exchange resin beads (Dowex 1X2, Fischer Scientific). The beads, which are supplied in Cl^- form, undergo a reversible reaction as



In a typical procedure, we prepare 100 ml of a 0.2 M solution of sodium fluorescein to which 15 g of ion-exchange beads is added under stirring. This loading of dye is close to the capacity of the ion-exchange beads and the dye solution is visibly depleted afterwards. We have observed that sodium fluorescein is not absorbed well onto resin beads in OH^- form.

Relevant physical properties of the dye-laden particles are presented in table 1. The mean particle radius $\langle a \rangle$ and standard deviation σ_a were obtained by processing microscope images taken at a resolution of 400 px mm^{-1} using a Hough-transform circle-detection routine. Statistics were based upon samples of 381 (50–100 mesh), 1350 (100–200 mesh) and 5152 (200–400 mesh) particles. While the larger 50–100 mesh particles exhibited little variation in size, the smallest 200–400 mesh particles had a relatively large coefficient of variation $\sigma_a/\langle a \rangle$ of around 24%. Particle density was measured in triplicate using a 5 ml pycnometric flask and an analytical balance with

Exchanger	$\langle a \rangle$ (μm)	$\sigma_a / \langle a \rangle$ (%)	ρ_p (kg m^{-3})	w_0 (mm s^{-1})	Re_w
Dowex 1X2 200–400	49.9	24	1199	1.07	0.11
Dowex 1X2 100–200	76.6	11	1201	2.45	0.37
Dowex 1X2 50–100	189.3	2	1192	10.81	4.08

Table 1. Properties of fluorescent dye-laden particles. Uncertainty in particle density is $\pm 2 \text{ kg m}^{-3}$. The quiescent settling velocity w_0 in water at 20°C was calculated based on the particle density ρ_p and mean radius $\langle a \rangle$ using (3.2).

10 mg resolution. The quiescent settling velocity in water at 20°C was calculated from

$$w_0 = \sqrt{\frac{g \langle a \rangle \rho_p - \rho_f}{3C_D \rho_f}} \quad (3.2)$$

based on the empirical drag coefficient relation

$$C_D = \frac{24}{Re_w} \left(1 + 0.1315 Re_w^{0.82 - 0.05 \log_{10} Re_w} \right), \quad (3.3)$$

which is applicable in the Reynolds number range $Re_w = 0.01\text{--}20$ (Clift, Grace & Weber 1978).

3.1.3. Shadowgraph and PLIF imaging

The combined shadowgraph and PLIF imaging set-up is shown in figure 2(a). In this, shadowgraph particle images are recorded by three Phantom v641 high-speed cameras, whilst PLIF images are recorded by the central camera only using illumination provided by a thin, continuous wave laser sheet. The shadowgraph and PLIF images are interleaved by time-multiplexing: pulsed backlight illumination is provided every other frame, so that frames recorded by the central camera alternate between PLIF and PLIF with shadows. Figure 2(b) shows an example of a sequential shadowgraph/PLIF image pair: particle shadows are visible over a wide depth of field, allowing for particle tracking, whilst dye fluorescence is only observed in the plane of the laser sheet.

Three coplanar cameras are used for 3-D particle tracking. The central camera is oriented normal to the laser sheet, whilst the side cameras view the flow near the centre of the tank at $\pm 30^\circ$ to the sheet normal. A set of 3-D-printed prisms with 2.5 mm thick acrylic windows allow the side cameras to view the flow without distortion across the air–PMMA–water interface. The shadowgraph backlight is provided by pulsed blue LEDs (Osram Golden DRAGON Plus), which are collimated by Sigma 105 mm lenses to evenly illuminate a small 13.7 cm^3 measurement volume at the centre of the tank. Particle shadows are imaged using a Nikon f/2.8 200 mm Macro lens, which achieves an optical magnification of almost 1 : 1. The spatial resolution in the PLIF measurement plane is $11.4 \mu\text{m px}^{-1}$. This illumination set-up means that the depth of field of the shadowgraph image is set by the collimation of the backlight, whereas the depth of field of PLIF imaging is set by the central camera’s aperture ($f_\# = 5.6$). To exclude the laser signal from the side cameras, we use a narrower aperture ($f_\# = 11$) so that any reflected light or fluorescent emission is very dim in comparison to the backlight.

Continuous-wave laser illumination is provided by a 1.1 W, Coherent Genesis MX laser at 514 nm. This choice of excitation wavelength is suboptimal for sodium fluorescein,

which has peak excitation at 494 nm, but provides satisfactory excitation of fluorescence. The beam is formed into a narrow laser sheet by a -10 mm focal length cylindrical lens and 350 mm spherical lens. The near-Gaussian beam quality ($M^2 = 1.06$) allows us to achieve a diffraction-limited beam waist of $w \approx 220 \mu\text{m}$. Because the PLIF excitation wavelength is close to the emission wavelength, we did not use a low-pass cut-off filter to isolate the fluorescence emission. Instead, we minimise the transmission of specular reflections from particles using a linear polariser on the central camera. Image acquisition is synchronised across cameras at a frame rate f_s with an exposure time of $250 \mu\text{s}$, which provided an acceptable compromise between motion blur and fluorescence signal intensity. The backlight pulse is much shorter ($\leq 35 \mu\text{s}$) so that position uncertainty due to motion blur of shadows is negligible. The frame rate was chosen to obtain a root-mean-square particle displacement of around 5–13 px between shadowgraph frames.

Calibration of the camera arrangement was performed using a $12 \text{ mm} \times 16 \text{ mm}$ chessboard calibration target with 1 mm squares laser-printed at 1200 dpi onto transparency film and transferred to a glass microscope slide. This was traversed across the measurement volume using a translation stage at $z = -10$ to 10 mm at 2 mm intervals. We then obtain a calibration using a standard pinhole camera model. Since the objective of these measurements is to visualise rather than quantify the scalar field, we did not calibrate fluorescence intensity against the dye concentration. However, we have confirmed with spectrophotometric measurements that the equilibrium dye concentration at the particle surface is $O(\mu\text{mol l}^{-1})$, so that the fluorescence emission is in the linear regime.

3.2. Particle tracking and wake reconstruction

Table 2 summarises the experimental conditions tested. From our previous PIV characterisation (Lawson & Ganapathisubramani 2022) and the particle properties in table 1, we compute the particle Stokes number St , turbulent Péclet number Pe , sinking ratio Sr and size relative to the Kolmogorov scale. Although the turbulent Péclet number is not controlled for in our experiments, the values are well within the convection-dominated regime ($Pe \gg 1$). It can be seen that the particles in our experiments are comparable to or smaller than the smallest dynamically active motions of the turbulent flow. For all cases, the characteristic turbulent acceleration $a_\eta = (\epsilon^3/\nu)^{1/4}$ is at least one order of magnitude smaller than the strength of gravitational acceleration, so slip due to turbulent acceleration is negligible. Furthermore, for the two smallest classes of particles, $St \ll 1$. By varying the turbulence intensity, we varied the sinking ratio Sr by an order of magnitude over the range in which the transition in mass transfer mechanism is expected to occur. For each condition, we obtained time series of 2738 (5000 at 2.4 kHz frame rate) shadowgraph and PLIF images, corresponding to between 1.9 and 6.8 s of turbulent motion, equivalent to approximately 1.3–3.2 integral time scales.

Lagrangian particle tracking was performed using an in-house code based on Lawson *et al.* (2018). This implements a low-density, predictor–corrector particle tracking algorithm following Ouellette, Xu & Bodenschatz (2006). The main difference is in particle image registration. Shadowgraph images are first levelised against a white image obtained from the 95th brightness percentile on a per-pixel basis. Subsequently, particle centres are identified using a Hough circle transform. Existing particle tracks are extrapolated linearly based on the last two frames and matched to the nearest corresponding particle centres (within a search radius of 20 px) and satisfying a triangulation tolerance (5 px). New tracks are initiated by triangulating unmatched particles and are extrapolated using a nearest-neighbour interpolation of the particle

Exchanger	f_l (Hz)	f_s (Hz)	$\epsilon \times 10^3$ ($\text{m}^2 \text{s}^{-3}$)	$u' \times 10^3$ (m s^{-1})	St	$\frac{\langle a \rangle}{\eta}$	$\frac{a_\eta}{g}$	Pe	Sr	Number of reconstructions
Dowex 1X2 200–400	1	400	0.015	11.0	3.7×10^{-3}	0.20	0.001	23	5.49	682
	2	800	0.21	29.0	1.4×10^{-2}	0.38	0.006	86	1.49	830
	4	1450	2.40	69.0	4.7×10^{-2}	0.70	0.035	290	0.44	1147
	6	2400	8.69	106.9	8.9×10^{-2}	0.97	0.092	560	0.23	1214
Dowex 1X2 100–200	1	400	0.015	11.0	8.8×10^{-3}	0.30	0.001	55	8.19	148
	2	800	0.21	29.0	3.2×10^{-2}	0.58	0.006	200	2.22	199
	4	1450	2.40	69.0	1.1×10^{-1}	1.08	0.035	690	0.65	359
Dowex 1X2 50–100	6	2400	8.69	106.9	2.1×10^{-1}	1.49	0.092	1300	0.34	1254
	2	800	0.21	29.0	2.0×10^{-1}	1.44	0.006	1200	3.96	181
	4	1450	2.40	69.0	6.7×10^{-1}	2.67	0.035	4200	1.16	755
	6	1450	8.69	106.9	1.3×10^0	3.68	0.092	8000	0.61	502

Table 2. Summary of experimental conditions.

velocity field, with a larger search tolerance. Tracks are terminated if a suitable match is not found or if matching is ambiguous.

We apply Taylor’s frozen flow hypothesis to reconstruct the scalar field in the vicinity of particles as they cross the laser sheet. In order to do this, we identify when particles cross the laser sheet based on their position and a calibrated model of the laser sheet plane. This plane is identified using the procedure illustrated in figure 3. When particles cross the laser sheet, we observe a sharp increase in their brightness due to their fluorescence as well as specular reflections, as shown in figure 3(a). We identify a set of crossing events based on a threshold, which define a set of points known to lie upon the laser sheet plane, as illustrated in figure 3(b). We use a robust fitting procedure to fit a plane to these points.

To reconstruct the 3-D scalar field, we identify the time t_0 when a particle trajectory $X(t)$ crosses the laser sheet plane $X(t_0) \cdot e_n + c = 0$. The PLIF images $I_{2D}(S + s, t)$ are then sampled in the vicinity of the projected position of the particle $S = P(X)$, where s is the two-dimensional (2-D) image coordinate relative to the particle centre and $P(x)$ represents the projection operation from 3-D object space to the 2-D image space of the camera. Images are sampled over ± 5 frames around each crossing event. Combined with the constraint that the fluorescence is emitted in the laser sheet plane, this allows us to reconstruct 11 planar slices of the scalar field $I_j(r)$ in the co-moving particle frame (2.5) for each crossing event j .

3.3. Results

Some representative examples of 3-D reconstructions of the scalar field in the co-moving particle frame are illustrated in the top row of figure 4. In these experiments, the particle type (and therefore the sinking speed) is held constant, whilst the dissipation rate (i.e. the characteristic rate of turbulent strain) is varied by changing the impeller speed. We observe that when the sinking ratio $Sr \gg 1$ (as in figure 4a), particles tend to have a single wake which is approximately aligned with the direction of sinking (r_2 axis). This indicates that slip is the dominant mechanism of convective mass transfer. We note, however, that the wake is not perfectly aligned with the direction of gravitational acceleration. When $Sr \ll 1$, the typical wake topology changes. Instantaneously, we observe examples of sheet-like

Mechanisms of mass transfer to spheres sinking in turbulence

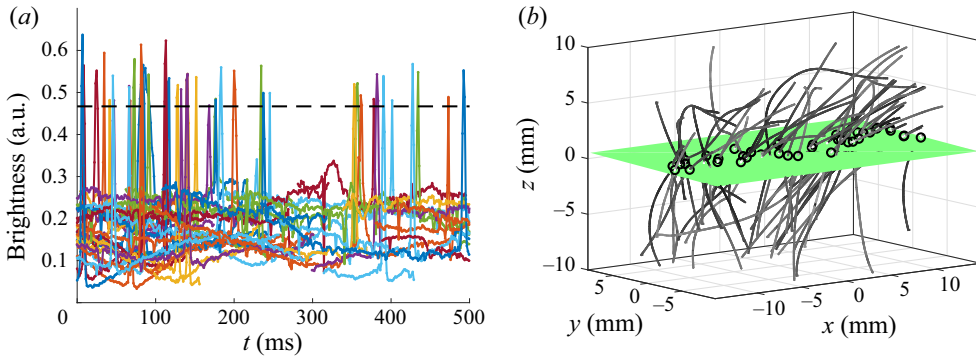


Figure 3. Identification of the laser sheet plane from particle trajectories. (a) An example of time-series measurements of particle brightness, showing the identification of particles which cross the laser sheet. (b) A 3-D reconstruction of the laser sheet plane (green), based on the position of identified crossings (black circles) of particle trajectories. Particle trajectories have been coloured according to their brightness. The white dotted line indicates the particle radius.

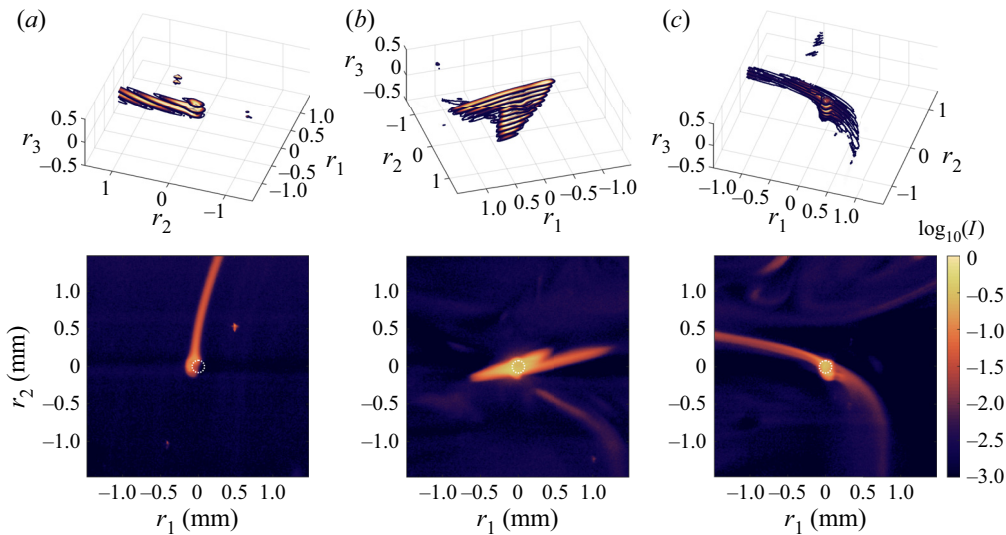


Figure 4. Reconstructions of the instantaneous scalar field in a co-moving frame around sinking, 100–200 mesh particles embedded in homogeneous turbulence: (a) $f_l = 1$ Hz, $Sr = 8.19$; (b,c) $f_l = 6$ Hz, $Sr = 0.34$. Upper panels show 3-D reconstructions of the scalar field. Lower panels show the 2-D projection of the scalar field as the particle transits the laser sheet. Sample video sequences of cases (a) and (b,c) are shown in supplementary movies 1 and 2, respectively. Gravitational acceleration is aligned with the $-r_2$ direction (particles sink in the direction of r_2 decreasing).

(figure 4b) and line-like (figure 4c) distributions of dye around the particle, which indicate that strain is the dominant mechanism of convective mass transfer. The bottom row of figure 4 shows the reconstructions projected in the laser sheet plane, i.e. averaged over the depth coordinate r_3 . In these, we see that sheet-like or line-like distributions of dye are projected with two wakes, whereas only one wake is visible in the slip-dominated case. As can be observed in supplementary movies 1 and 2, these asymmetric single-wake or symmetric double-wake structures are common in these limiting cases.

To characterise the average topology of the surrounding wake in the co-moving frame, we evaluated the ensemble-average 2-D projection of the reconstructed scalar field $\langle I_j(\mathbf{r}) \rangle_z$ for all crossing events j . This is shown in [figure 5](#). We observe that, when the sinking ratio is large ([figure 5a–c](#)), there is a clear signature of the concentration wake created by gravitational slip. However, as the sinking ratio is decreased, the mean distribution of dye around the particle becomes more isotropic. This effect is most pronounced at the smallest sinking ratio (e.g. [figure 5j,k](#)). This demonstrates that the mass transfer cannot be explained by gravitational settling alone when the sinking ratio is $O(1)$ or smaller: turbulent shear, acceleration and strain may all act to isotropise the mean distribution of scalar around the particle. Evident in [figure 5](#) is also an artefact of our imaging method: images are dimmer on the right-hand side where a shadow has been cast by the particle. Due to the background subtraction we apply, which subtracts the average intensity over the r_1 direction, the signal of the unshadowed portion of the laser sheet is also artificially increased.

To identify a change in the mechanism of mass transfer, we repeat our analysis in a coordinate system aligned with the particle wake. To do this, we define a polar coordinate system (r, θ) for the projected scalar field $I_{2D}(r, \theta) = \langle I(\mathbf{r}) \rangle_z$ such that $r_1 = r \cos \theta$, $r_2 = r \sin \theta$. We identify the angle $\theta_{m,i}$ at which $I_{2D}(2 \langle a \rangle, \theta)$ is maximised, i.e. we identify the instantaneous orientation of the wake at the radius shown in [figure 5](#). We then evaluate the average scalar field in this in a new, wake-aligned relative coordinate system (r, θ') , where $\theta' = \theta - \theta_{m,i}$ and $r'_1 = r \cos \theta'$, $r'_2 = r \sin \theta'$. The result is shown in [figure 6](#). We observe that, when the sinking ratio is large (e.g. [figure 6a–f](#)), the average wake-aligned field shows a single wake. However, when the sinking ratio is small (e.g. [figure 6g,j,k](#)), a second concentration wake appears on the opposite side of the particle. This is consistent with the expected distribution of scalar for particles with strain-dominated mass transfer (see [figures 9](#) and [4](#)). A second wake structure is not observed on average for the largest 50–100 mesh particles with $Re_w > 1$, but this may be because our experiments do not reach sufficiently small Sr (compare e.g. [figure 6h,i](#)). Therefore, our laboratory flow visualisations confirm a change in the mechanism of mass transfer for particles in the Stokes regime ($Re_w < 1$) as the sinking ratio is varied.

4. Numerical simulations

Our experiments have confirmed that a transition in the mechanism of mass transfer occurs as the sinking ratio is varied. However, they do not allow us to quantify the relative contributions of convection due to strain and slip. In this section, we extend the approach developed in Lawson & Ganapathisubramani (2021) to simulate the mass transfer from a dilute suspension of sinking particles by incorporating a slip velocity. This will allow us to quantify in detail the relative roles of the two mechanisms. The basic idea is to force (2.8) using the Lagrangian time history of the relative velocity field perceived by sinking point-particles in a direct numerical simulation of homogeneous, isotropic turbulence. The convection–diffusion problem is solved numerically on a boundary-fitted domain in a reference frame co-moving and co-rotating with the particle. The grid is sufficiently refined to resolve the development of the concentration boundary layer near the particle surface. The domain is truncated far from the particle and the inflow boundary condition there models incoming fluid as uncontaminated, so that the turbulence effectively provides a continuous supply of fresh fluid. This method retains the advantage of particle-resolved direct numerical simulation (Feng & Michaelides 2009; Deen *et al.* 2014) that the concentration boundary layer surrounding the particle is resolved, but disregards larger-scale mixing and turbulent transport.

Mechanisms of mass transfer to spheres sinking in turbulence

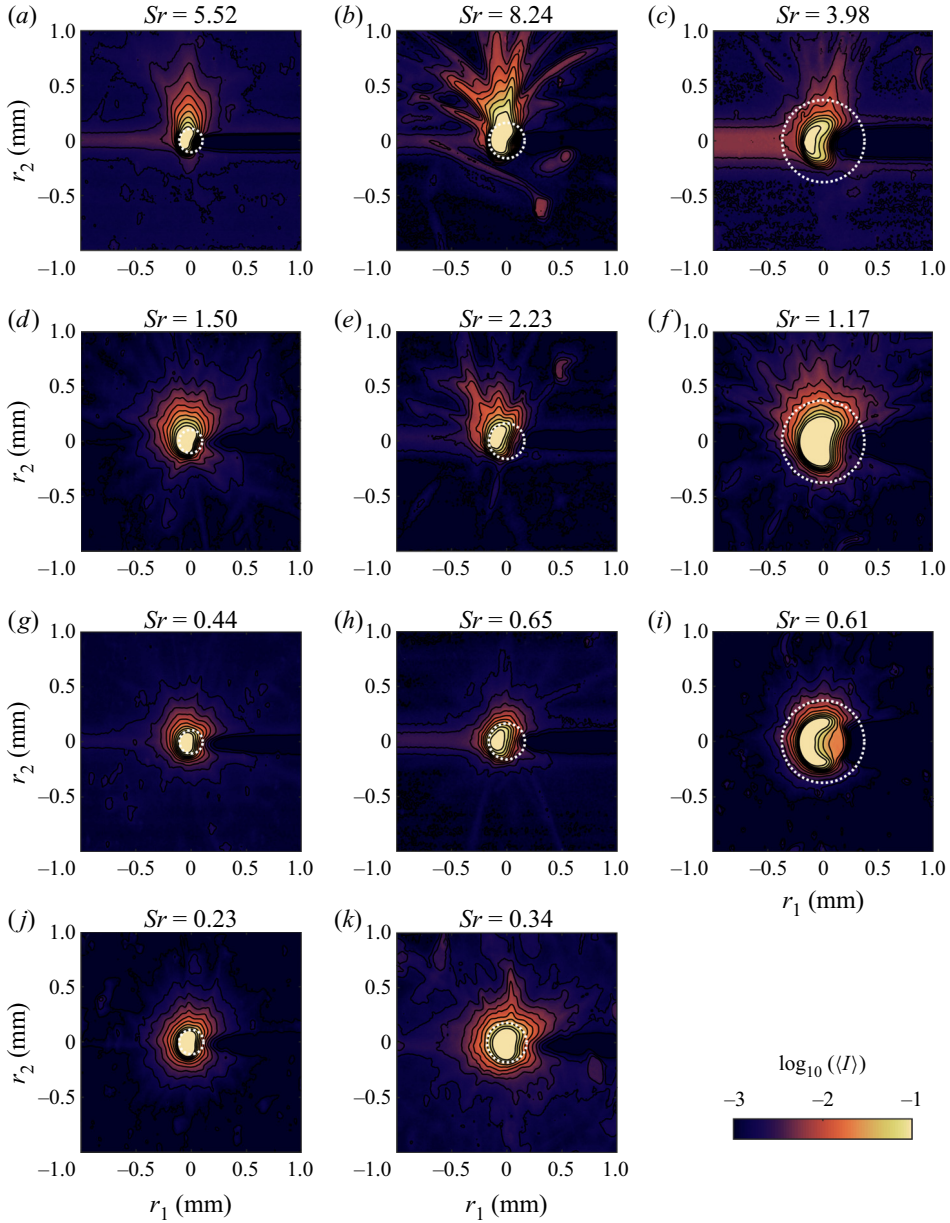


Figure 5. Two-dimensional projections of the mean scalar field around sinking particles embedded in homogeneous turbulence, evaluated in the laboratory-aligned co-moving frame: (a,d,g,j) 200–400 mesh ($\langle a \rangle = 50 \mu\text{m}$), $\epsilon = 15\text{--}8690 \text{ mm}^2 \text{ s}^{-2}$; (b,e,h,k) 100–200 mesh ($77 \mu\text{m}$), $\epsilon = 15\text{--}8690 \text{ mm}^2 \text{ s}^{-2}$; (c,f,i) 50–100 mesh ($190 \mu\text{m}$), $\epsilon = 210\text{--}8690 \text{ mm}^2 \text{ s}^{-2}$. The dashed white circle shows $r = 2$ (a).

4.1. Numerical methodology

The numerical procedure to implement the model is similar to that of Lawson & Ganapathisubramani (2021). We summarise the details here only briefly. The trajectories of particles sinking in homogeneous, isotropic turbulence at $R_\lambda = 433$ are obtained from the Johns Hopkins Turbulence Database (Li *et al.* 2008). Ensembles of 1000 Lagrangian particles are uniformly seeded throughout the simulation domain at time $t = 0$ and their

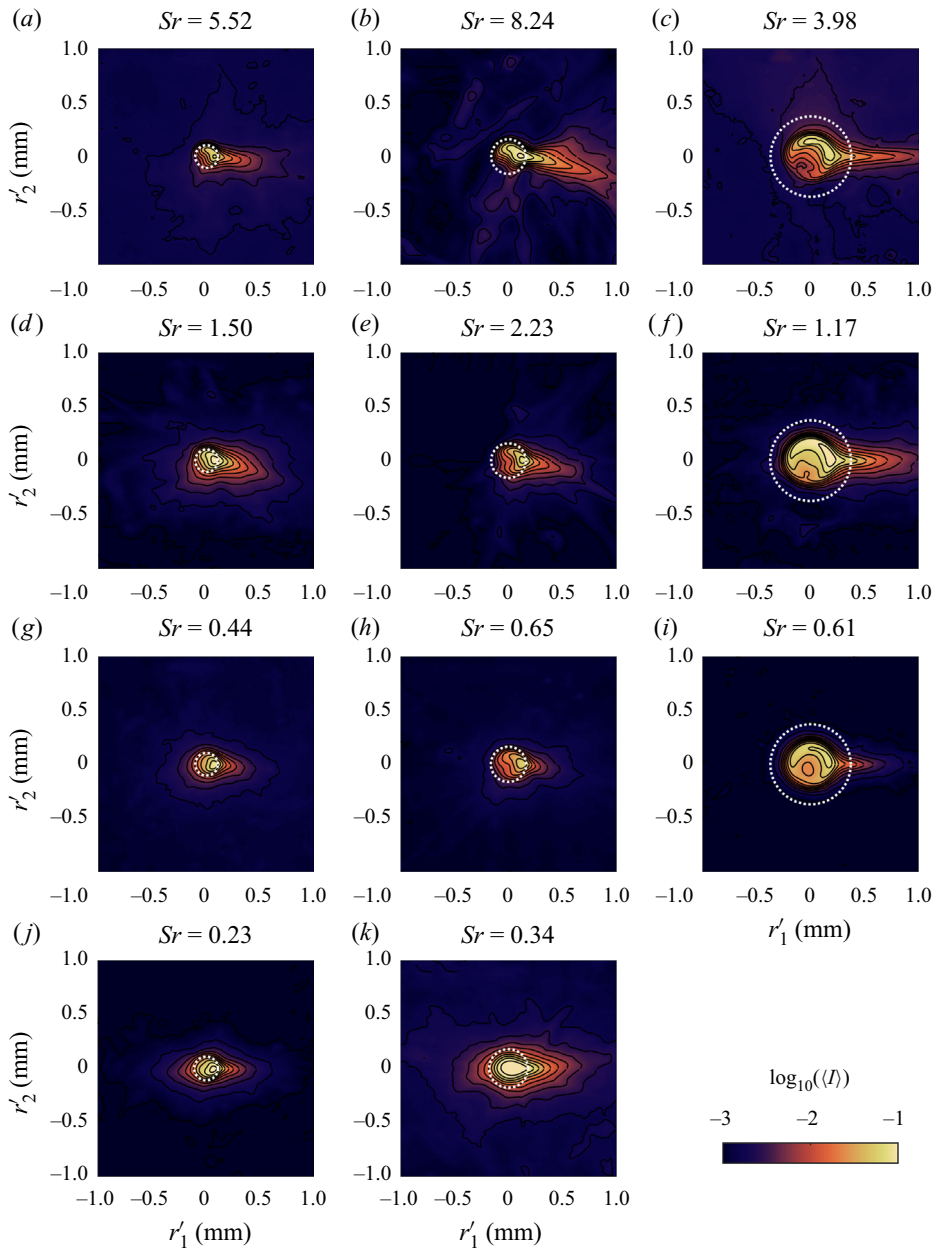


Figure 6. Two-dimensional projections of the mean scalar field around sinking particles embedded in homogeneous turbulence, evaluated in the wake-aligned co-moving frame: (a,d,g,j) 200–400 mesh ($(a) = 50 \mu\text{m}$), $\epsilon = 15\text{--}8690 \text{ mm}^2 \text{ s}^{-2}$; (b,e,h,k) 100–200 mesh ($77 \mu\text{m}$), $\epsilon = 15\text{--}8690 \text{ mm}^2 \text{ s}^{-2}$; (c,f,i) 50–100 mesh ($190 \mu\text{m}$), $\epsilon = 210\text{--}8690 \text{ mm}^2 \text{ s}^{-2}$. The dashed white circle shows $r' = 2$ (a).

trajectories are integrated as

$$\dot{X} = \mathbf{u}(X(t), t) + \mathbf{w}_0, \quad (4.1)$$

where the settling velocity is given by (2.3). Equation (4.1) is integrated over the duration of the simulation $T_{sim} = 10.056$ using a second-order Runge–Kutta scheme with a time

step $\Delta t = 0.002 \approx 0.047\tau_\eta$, corresponding to the time resolution of the database. The velocity and velocity gradient are interpolated from the database at the tracer position using a fourth-order Lagrange polynomial interpolation. This yields a time series of the local velocity gradient $\mathbf{G}(\mathbf{X}, t_i)$ at $i = 0 \dots 5028$ times $t_i = i\Delta t$. The orientation of the body frame $\mathbf{R}(t)$ (2.6) is integrated from an initially random (isotropic) orientation using an adaptive time step, third-order Runge–Kutta scheme using a piecewise, linear interpolation to interpolate $\mathbf{G}(\mathbf{X}, t)$. This provides time series of the particle–fluid relative velocity $\mathbf{v}_0(t)$ and gradient $\mathbf{E}(t)$ in the co-rotating frame.

We track the motion (4.1) of seven separate ensembles of spherical particles with the same initial position but different sinking rates $w_0/u_\eta = (a/\eta)Sr = 10^{-3}–10^0$. Although w_0/u_η is small, the difference in sinking rate can build up into a large difference in trajectory over time. From these we obtain the Lagrangian relative velocity history (2.11) of two sizes of small spheres $a/\eta = 10^{-2}$ and 10^{-1} at differing sinking ratio $\log_{10} Sr = -1, -0.5, 0, 0.5, 1$.

We then solve the convection diffusion problem (2.8) numerically using a modified version of OpenFOAM scalarTransportFoam solver used in Lawson (2021) and Lawson & Ganapathisubramani (2021). This implements a second-order finite-volume solver for θ , with a standard linear upwind Gaussian discretisation of the convective term in (2.8) and linear Gaussian scheme for the diffusive term with explicit non-orthogonal correction to maintain second-order accuracy. Convective forcing (2.11) is implemented by specifying the relative velocity field as the superposition of Stokes flow solutions, obtained from analytical expressions given in Kim & Karrila (1991). Equation (2.8) is discretised onto a structured grid in spherical coordinates (r, ψ, ϕ) with $150 \times 64 \times 64$ cells, where r is the radial coordinate, ψ is the polar coordinate and ϕ the azimuthal. Cells are spaced uniformly in the azimuthal direction $\phi_i = 0 \dots 2\pi$ and polar direction $\cos \psi_i = -1 \dots 1$. To adequately resolve the thin concentration boundary layer, we employ a mesh refinement $\Delta r_{i+1} = \alpha r_i$, where $\Delta r_i = r_{i+1} - r_i$ is the spacing between cells in the radial direction. We choose $\alpha = 1.0724$. Based on an estimated boundary layer thickness $\delta = Pe_w^{-1/3}$ at the largest Péclet number ($Pe_w = 10^5$, $Pe = 10^4$) tested, there are at least 32 cells within a distance δ from the surface. We impose the Dirichlet boundary condition $\theta = 1$ at the particle surface $r/a = 1$ and the Neumann boundary condition on the outer surface $r/a = 100$ to approximate the zero-concentration boundary far from the particle. Time stepping is performed using an implicit Euler scheme with a time step $\Delta t^* = 0.0236$ from the initial condition $\theta(\mathbf{y}^*, 0) = 0$.

As in Lawson & Ganapathisubramani (2021), there is an initial transient in the ensemble-average mass transfer rate $\langle Sh \rangle$ obtained from the simulation, which corresponds to the diffusive growth of the concentration boundary layer. An example of this transient is provided in Appendix A, where a stationary state can be observed by $t^* > 75$. Averaging over the time interval $75 < t^* < T_{sim}^*$, the deviation of the ensemble average $\langle Sh \rangle$ from the time average $\overline{\langle Sh \rangle}$ does not exceed 2% and the statistical uncertainty in $\overline{\langle Sh \rangle}$ is below $\pm 0.5\%$ (based on a 95% confidence interval).

4.2. Average mass transfer rate

We first examine the average mass transfer rate predicted by our numerical simulations. Figure 7(a) shows the ensemble-average mass transfer rate to sinking particles of different sizes as a function of the turbulent Péclet number Pe and sinking ratio Sr . We observe that the average mass transfer rate is insensitive to the particle size relative to the Kolmogorov scale ($a/\eta = 10^{-2}, 10^{-1}$), provided the sinking ratio Sr is held constant. The square

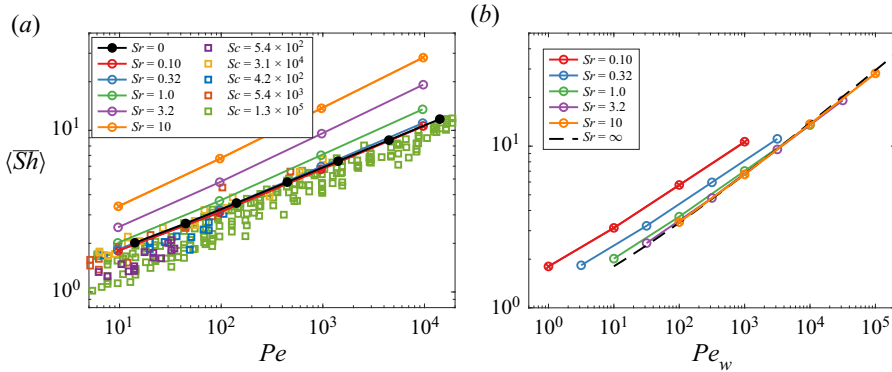


Figure 7. Ensemble-average Sherwood number as a function of (a) turbulent Péclet number Pe and (b) quiescent settling Péclet number Pe_w . The markers correspond to: simulations with $a/\eta = 10^{-2}$ (\circ) and 10^{-1} (\times); experimental data of small spheres (\square) with $St < 0.1$ and $Sr < 0.12$ from Armenante (1983). The dashed line corresponds to the asymptotic expression (4.2) for small particles sinking in quiescent flow (Acrivos & Goddard 1965).

markers in figure 7(a) show experimental measurements of the mass transfer rate to small spheres in turbulence with $St < 0.1$ and $Sr < 0.12$ obtained from data tabulated in Armenante (1983) and later reported in Armenante & Kirwan (1989). At small $Sr = 0.1$, our numerical simulations are in good agreement with the experimental data. For fixed Pe , a significant enhancement in convective mass transfer is seen as Sr is increased beyond $Sr \approx 0.33$.

Figure 7(b) shows the same simulation data as a function of the quiescent settling Péclet number Pe_w . When convection due to sinking is strong in comparison with the turbulence (i.e. $Sr \gg 1$), the data approach the high-Péclet-number asymptotic expression

$$Sh = 0.6245Pe_w^{1/3} + 0.461 + O(Pe_w^{-1/3}) \tag{4.2}$$

for small particles in uniform flow (Acrivos & Goddard 1965). By comparing data at similar Pe_w but different Sr , we note that the general trend is for strong turbulence (i.e. $Sr < 1$) to increase the mass transfer rate compared to sinking alone. However, at the very largest Péclet numbers $Pe_w \geq 10^4$, we observe a small but statistically significant decrease (0.20 ± 0.035 , or around 1.5 %) in $\langle Sh \rangle$ at $Sr = 1$ compared with $Sr = 10$. This is consistent with the assertion of Batchelor (1980) that, for fixed $Pe_w \gg 1$, the effect of turbulent stirring should initially decrease the average rate of mass transfer. Figures 7(a) and 7(b) therefore demonstrate that Sr effectively interpolates between two regimes of mass transfer: strain-dominated, where $Sr \ll 1$ and the mass transfer rate primarily depends upon the turbulent strain rate; and slip-dominated, where $Sr \gg 1$ and convective mass transfer is determined by the slip velocity.

This observation raises the possibility of finding an empirical function which smoothly interpolates between these two limiting regimes. Motivated by the success of previous empirical expressions of the form (1.1) with $\beta = 1/2$ and $\gamma = 1/3$ (Frössling 1938; Ranz & Marshall 1952), we plot the normalised mass transfer rate $(\langle Sh \rangle - 1)/Pe^{1/3}$ as a function of the sinking ratio in figure 8. Although this normalisation does not incorporate the anomalous Péclet number scaling we have observed due to the convection-suppression effect (Lawson & Ganapathisubramani 2021), we find it provides a satisfactory collapse of

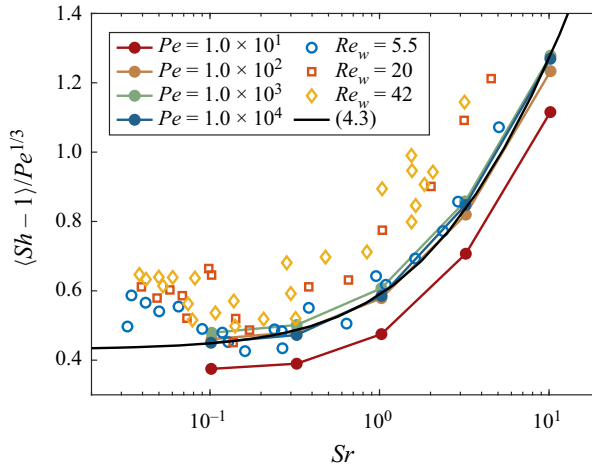


Figure 8. Normalised mass transfer rate $\langle Sh - 1 \rangle / Pe^{1/3}$ shown as a function of the sinking ratio Sr . Filled markers correspond to numerical simulation data at fixed Pe , whereas open markers correspond to experimental data at fixed Pe_w digitally extracted from Ohashi *et al.* (1981). The solid black line shows the best fit of our simulation data to (4.3) over the range $10^2 \leq Pe \leq 10^4$.

our data over $10^2 \leq Pe \leq 10^4$. A fit to the data in this range of the form

$$Sh = 1 + Pe^{1/3} \frac{(\alpha' Sr + \beta')^{4/3}}{Sr + \gamma'} \tag{4.3}$$

with $\alpha' = 0.6245^{3/4}$ provides the asymptotic scaling (4.2) at large Sr accurate to leading order in Pe_w . The coefficients $\beta' = 1.293$ and $\gamma' = 3.269$ are chosen by minimising the sum of squares error in $\langle Sh \rangle$. The fit to our numerical data in this range is good, with the largest residual being 5.2%.

Compensating for Péclet number in this manner, we are also able to directly compare our numerical simulations with the experimental data of Ohashi *et al.* (1981), who measured the mass transfer rate from freely suspended spherical particles sinking in vertical turbulent pipe flow. In these experiments, three sizes of spherical ion-exchange particles were injected into a vertical turbulent pipe flow containing a sodium hydroxide electrolyte. The mass transfer was determined by the diffusion-limited exchange of sodium/potassium cations, measured by atomic absorption analysis. The mass transfer coefficient $k = ShD/a$ was determined at fixed $Sc = 368$ for varying bulk upflow velocity U_b , and therefore varying turbulent dissipation rate $\epsilon = 2fU_b^3/D_p$, where f is the Fanning friction factor and D_p is the pipe diameter. The quiescent sinking Reynolds and Péclet numbers span $Re_w = 5.5, 20, 42$ and $Pe_w = 1.0 \times 10^3, 3.6 \times 10^3, 7.7 \times 10^3$. We digitally extracted the mass transfer coefficient k and bulk flow velocity U_b from their figure 1 and computed the quiescent sinking velocity of their ion-exchange particles using (3.2). Following Ohashi *et al.* (1981), we obtained the friction factor from the Blasius correlation $f = 0.079(U_b D_p / \nu)^{-1/4}$. The quantitative agreement at the smallest $Re_w = 5.5$ is good, despite this being beyond the Stokes regime of our simulation. The quantitative agreement at larger Reynolds numbers is fair, but shows the same trends. This is expected, given the reported Reynolds-number dependence of mass transfer in uniform flow and the well-established appearance of a wake recirculation zone at $Re_w \approx 20$ (Clift *et al.* 1978). These observations provide further confidence in our numerical simulation approach and confirm the existence of a transition in the mass transfer mechanism parametrised by Sr .

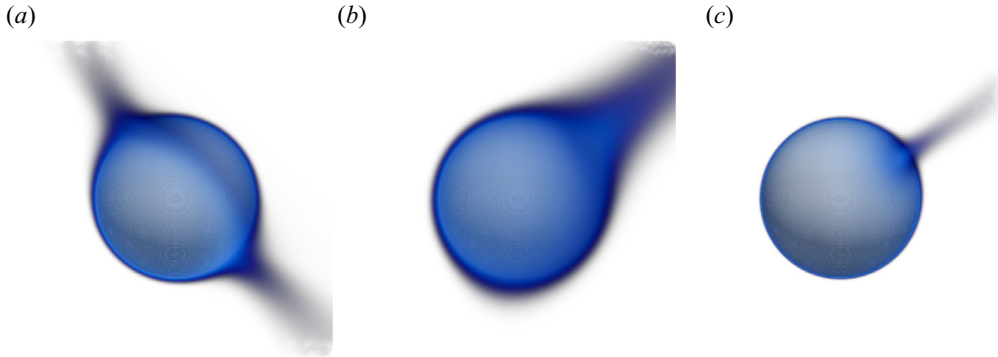


Figure 9. Visualisation of the concentration boundary layer and wake around a spherical particle at $Pe = 10^4$ and $a/\eta = 10^{-2}$ with (a) $Sr = 0.1$, (b) $Sr = 1$ and (c) $Sr = 10$. The visualisation shows the concentration field around a particle at $t^* = 100$, which was seeded at the same position at $t^* = 0$ but subject to different sinking rates.

4.3. Mechanism of mass transfer

Figure 9 presents a visualisation of the concentration boundary layer and wake around a simulated particle as the sinking ratio is increased. When $Sr = 0.1$, fluid is swept approximately along streamlines into two, nearly symmetric wakes. This closely resembles the topology of the concentration field expected under steady, extensional strain. As the sinking ratio is increased, the topology of the wake changes towards a single wake in a near-uniform flow field. This closely resembles the topology of the concentration field expected under steady, uniform flow driven by slip. We therefore qualitatively confirm the existence of a transition in the dominant mass transfer mechanism between the small and large Sr regimes.

To examine the transition in mass transfer mechanism quantitatively, we consider a budget of the diffusive, convective and unsteady solute fluxes in a control volume surrounding the particle. The flow field relative to the particle (2.7) can be decomposed into linear contributions $\mathbf{v} = \mathbf{v}_\epsilon + \mathbf{v}_w$ from the relative slip due to gravity \mathbf{v}_w and strain \mathbf{v}_ϵ imposed by turbulent eddies. For a spherical shell control volume $\mathcal{V} = \{\mathbf{y} : a \leq |\mathbf{y}| \leq r\}$ with variable outer radius r , we obtain the temporally averaged balance of convective and diffusive solute fluxes from (2.8) as

$$A^* + Q_\epsilon^* + Q_w^* + Q_D^* - 4\pi \overline{\langle Sh \rangle} = 0, \tag{4.4}$$

where we have defined

$$\left. \begin{aligned} A^*(r^*) &= \int_{\mathcal{V}} \left\langle \frac{\partial \theta}{\partial t^*} \right\rangle d\mathbf{y}, \\ Q_\epsilon^*(r^*) &= \int_{|\mathbf{y}^*|=r^*} \overline{\langle \mathbf{v}_\epsilon^* \theta \rangle} \cdot d\mathbf{S}, \quad Q_w^*(r^*) = \int_{|\mathbf{y}^*|=r^*} \overline{\langle \mathbf{v}_w^* \theta \rangle} \cdot d\mathbf{S}, \\ Q_D^*(r^*) &= -\frac{1}{Pe} \int_{|\mathbf{y}^*|=r^*} \nabla_{\mathbf{y}^*} \cdot \overline{\langle \theta \rangle} \cdot d\mathbf{S}, \end{aligned} \right\} \tag{4.5}$$

in conjunction with the boundary condition $\mathbf{v} = \mathbf{v}_w = \mathbf{v}_\epsilon = 0$ on $r = a$. Numerically, this is obtained through volume integrals of the convection–diffusion terms in (2.8), which is solved using a conservative, finite-volume method. Thus, mass conservation is implicitly satisfied. The terms in (4.4) can be understood as follows. The diffusive flux of material

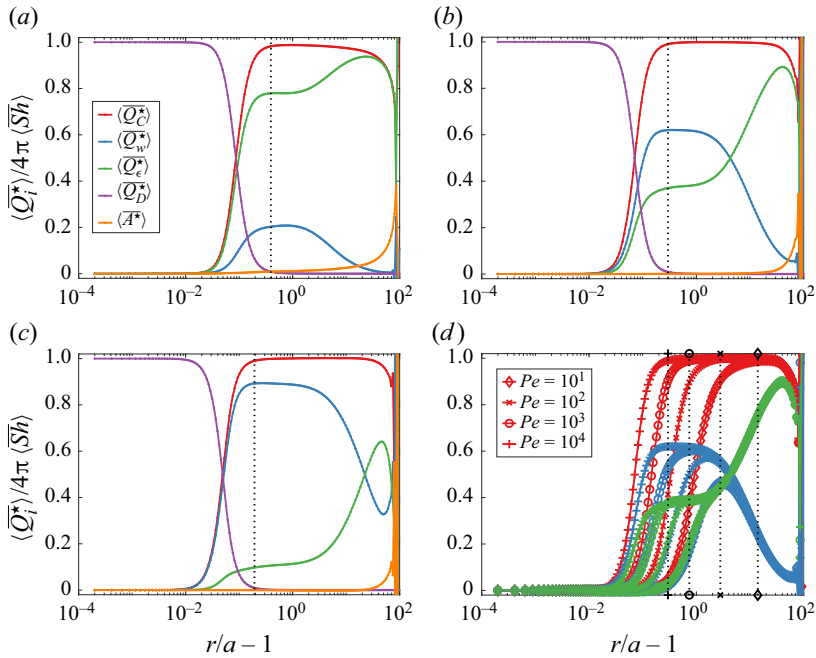


Figure 10. Decomposition of the scalar transport from a spherical particle as a function of control volume radius r/a at $a/\eta = 10^{-2}$. (a–c) Full breakdown of unsteady, diffusive and convective terms in (4.4) for $Pe = 10^4$ and (a) $Sr = 0.32$, (b) $Sr = 1.0$ and (c) $Sr = 3.2$. The black dotted line indicates $r = a + \delta_D$, where $Q_D^*(r)/4\pi \langle \bar{Sh} \rangle = 0.01$. (d) Breakdown of convective terms only for $Pe = 10^1-10^4$ and $Sr = 1.0$. Markers indicate the turbulent Péclet number, whilst colour indicates terms as in (a–c).

into \mathcal{V} from the particle surface is $4\pi \langle \bar{Sh} \rangle$. This must be balanced by the convective flux due to slip Q_w^* and strain Q_ϵ^* , the diffusive flux Q_D^* at $|y| = r$ or the time-average unsteady accumulation A^* of material within \mathcal{V} . Because $\mathbf{v}_w(\mathbf{y}, t) = \mathbf{v}_w(-\mathbf{y}, t)$ is even in \mathbf{y} , only the odd, parity-antisymmetric component of $\theta(\mathbf{y}, t)$ contributes to the convective flux due to slip (4.5). Likewise, since the strain component $\mathbf{v}_\epsilon(\mathbf{y}, t) = -\mathbf{v}_\epsilon(-\mathbf{y}, t)$ is odd in \mathbf{y} , only the parity-symmetric, even component of $\theta(\mathbf{y}, t)$ contributes to the convective flux due to strain.

Figure 10(a–c) shows the balance of these terms (4.4) in the mass transport away from a spherical particle at $Pe = 10^4$ and $Sr = 0.32, 1.0$ and 3.2 . The sum of the convective terms $Q_C^* = Q_w^* + Q_\epsilon^*$ is also shown. Near the particle, diffusion dominates mass transfer; far from the particle, the diffusive flux Q_D^* vanishes by construction at the boundary condition $r/a = 100$. We therefore define a diffusion thickness, δ_D , such that $Q_D^*(a + \delta_D) = 0.01(4\pi \langle \bar{Sh} \rangle)$. This defines a measure of the thickness of the concentration boundary layer, at the edge of which the diffusive flux of solute away from the particle is negligible. We note that this is analogous to defining a 99% thickness in terms of the scalar gradient $\nabla_\star \langle \bar{\theta} \rangle$. Beyond this scale, convection dominates the mass transfer out of \mathcal{V} and the control volume is in equilibrium, i.e. the unsteady accumulation of material is negligible. At very large $r/a \approx 58$, the equilibrium approximation breaks down and the unsteady accumulation of material accounts for over 10% of the solute flux from the particle. This is expected given the finite run-time of our simulation. Nonetheless, we are able to observe a wide range of scales over which convection $Q_C^* \approx 4\pi \langle \bar{Sh} \rangle$ balances the diffusive flux from the particle surface.

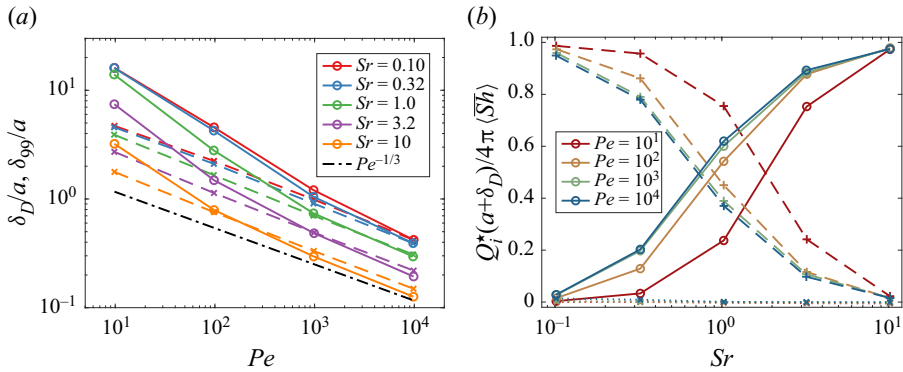


Figure 11. (a) The variation of the concentration boundary layer thickness based on the diffusive flux thickness δ_D and the 99 % thickness δ_{99} with turbulent Péclet number and sinking ratio. (b) The breakdown of fluxes due to strain (Q_ϵ^* , dashed line), slip (Q_w^* , solid line) and unsteady accumulation (A^* , dotted line) at the edge of the concentration boundary layer $r = a + \delta_D$, as a function of the sinking ratio Sr . Colours correspond to varying turbulent Péclet number.

By comparing figure 10(a–c), we discern the effect of the sinking ratio upon the mechanism of convective mass transfer away from the particle. At large turbulent Péclet number, we identify a large range of scales over which convection dominates the mass transfer away from the particle. The lower end of this range corresponds to the thickness of the concentration boundary layer, δ_D , whilst the upper end of this range is limited by the time needed for our simulation to reach equilibrium. Across this range, the balance between the convective flux due to slip Q_w^* and strain Q_ϵ^* is not uniform. In all cases, convection by strain dominates the solute flux away from the particle at large scales. However, there exists a subrange of scales over which the relative contributions of convection due to strain and slip are approximately constant. The lower extent of this range corresponds to the diffusive thickness of the concentration boundary layer, δ_D , whereas the upper extent of this range increases as the sinking rate Sr is increased.

The balance of convection and diffusion across scales also depends upon the turbulent Péclet number, as shown in figure 10(d). As the turbulent Péclet number is increased, the concentration boundary layer thins and we observe an increasing range of scales over which convection dominates the mass transfer away from the particle. The relative contributions of the convective fluxes exhibit a remarkable collapse beyond $r/a \approx 3$ for $Sr = 1$. Figure 11(a) shows the thickness of the concentration boundary layer in terms of the conventional 99% thickness δ_{99} and the diffusion layer thickness δ_D . We observe that the two definitions provide comparable measures of the boundary layer thickness and converge towards similar values at large Pe . The data are also in agreement with the expected $\delta_{99} \sim Pe^{-1/3}$ scaling at large Pe , although the range over which this scaling is applicable is arguably only valid for $Pe > 10^3$ such that $\delta_{99}/a \ll 1$.

From our discussion so far, we have seen that the mechanism of convective solute transport away from the particle depends upon scale. We have also seen that the diffusion thickness δ_D serves as a measure of the thickness of the concentration boundary layer, which lies within a region where convection is dominant and the relative contributions due to slip and strain are approximately independent of r . It is therefore instructive to compare the relative contribution of these convective fluxes within this range. Figure 11(b) shows this balance at $r = a + \delta_D$. By definition, diffusion accounts for 1% of the normalised flux at this location. As the turbulent Péclet number is increased, the relative contributions of each of these mechanisms approaches an asymptotic value. As the sinking ratio is

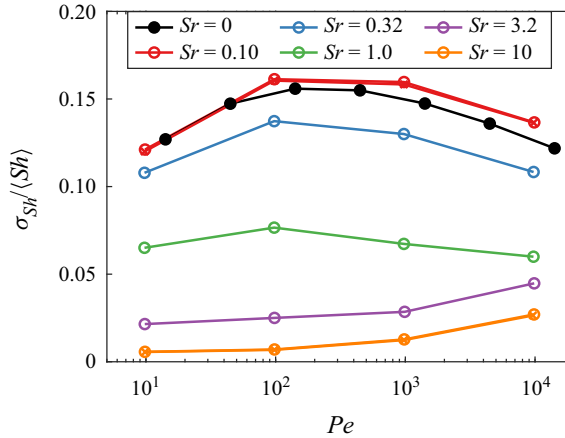


Figure 12. Standard deviation σ_{Sh} of fluctuations in the local mass transfer rate Sh , relative to the mean, as a function of the turbulent Péclet number and sinking ratio Sr . The open markers correspond to simulations with $a/\eta = 10^{-2}$ (\circ) and 10^{-1} (\times); the black filled markers show data for spherical particles at $Sr = 0$ from Lawson & Ganapathisubramani (2021).

increased, there exists a transition in the mechanism of convective mass transfer at the edge of the concentration boundary layer: at $Sr = 0.1$, virtually all mass transfer is attributable to the turbulence; at $Sr = 10$, virtually all mass transfer occurs due to slip. Around $Sr \approx 1$, the contributions are comparable. This quantitatively demonstrates a change in the mechanism of mass transfer at the scale of the particle from strain-dominated to slip-dominated as the sinking ratio Sr is increased.

4.4. Fluctuations in the mass transfer rate

Thus far, we have examined only the average rate of mass transfer from the particle. We now turn our attention to the fluctuations in the mass transfer rate and their correlation with the convective forcing. Figure 12 shows the magnitude of the mass transfer fluctuations with respect to the mean as a function of the turbulent Péclet number and sinking ratio. At small sinking ratio $Sr \ll 1$, we observe first an increase in the magnitude of the mass transfer fluctuations with increasing Pe , with a shallow peak around $Pe \approx 10^2$ – 10^3 , followed by a decrease in fluctuation magnitude with increasing Pe . This is consistent with the behaviour we have observed for neutrally buoyant spherical and spheroidal particles, which arises from the convection-suppression effect (Lawson & Ganapathisubramani 2021). The relative magnitude of Sh fluctuations is slightly larger in the weakly sinking case $Sr = 0.1$ compared with our previous data at $Sr = 0$; the difference is larger than the statistical uncertainty in the data. As the sinking ratio is further increased, the relative magnitude of the mass transfer fluctuations is decreased. Furthermore, the Pe dependence is also changed. At the largest sinking rates $Sr = 3.2, 10$ we observe a monotonic increase in the fluctuation magnitude with increasing Pe . However, the magnitude of these fluctuations remains quite small (2%–5% of the mean) at the largest turbulent Péclet numbers tested.

For sinking particles, turbulence introduces fluctuations in the solution of (2.8) through two mechanisms. Firstly, fluctuations in strain \mathbf{E} may directly cause fluctuations in the mass transfer rate. Secondly, although the particle sinks at a constant rate w_0 in the laboratory frame, turbulence causes the particle to rotate with angular velocity $\boldsymbol{\Omega} = \boldsymbol{\omega}/2$.

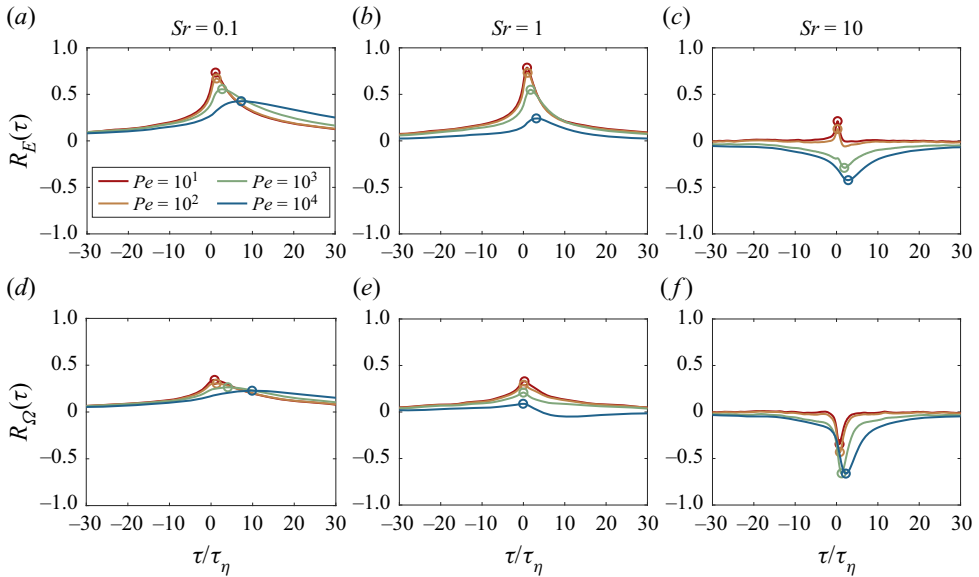


Figure 13. Cross-correlation function of the instantaneous mass transfer rate $Sh(t + \tau)$ against (a–c) local strain magnitude $E(t)$ and (d–f) local rotation rate $\Omega_\perp(t)$ at time t . Line colours correspond to different turbulent Péclet numbers. The circular markers indicate the time lag τ at which the cross-correlation is maximised.

Therefore, the slip velocity in the particle frame \mathbf{v}_0 also fluctuates in time, since $\mathbf{v}_0 = -w_0 \mathbf{R}^T(\boldsymbol{\Omega} \times \mathbf{e}_z)$. The magnitude of these fluctuations is therefore determined by the rate of rotation $\Omega_\perp = |\boldsymbol{\Omega} \times \mathbf{e}_z|$ perpendicular to the direction of gravity. The two mechanisms may have significant correlation with each other, since the strain rate E and vorticity magnitude $|\boldsymbol{\omega}|$ are strongly correlated in homogeneous turbulence (Zeff *et al.* 2003). Indeed, in our data, we find that E and Ω_\perp are interdependent with product-moment correlation coefficient $R_{E\Omega} \approx 0.54$.

In figure 13, we present the cross-correlation functions $R_E(\tau)$ and $R_\Omega(\tau)$ between the instantaneous mass transfer rate $Sh(t + \tau)$ evaluated at a time lag τ relative to the strain $E(t) = |\mathbf{E}|$ (figure 13a–c) and rotation rate $\Omega_\perp(t)$ (figure 13d–f). For $Sr = 0.1$, where the average mass transfer rate is dominated by strain, we observe that the strain E is strongly, positively correlated with the instantaneous transfer rate. There is also a weaker, positive correlation with the rotation rate Ω_\perp . As the turbulent Péclet number is increased, the local transfer rate correlates less strongly with the local strain rate (and rotation rate) and over a longer time scale. A similar behaviour can also be observed at $Sr = 1$. This is an example of the convection-suppression effect, where the concentration boundary layer becomes unresponsive to velocity fluctuations occurring on time scales faster than $O(\tau_\eta Pe^{1/3})$, in agreement with simulations of neutrally buoyant spheroids (Lawson & Ganapathisubramani 2021).

On the other hand at $Sr = 10$, where the average mass transfer rate is dominated by slip, fluctuations in the mass transfer rate are strongly, negatively correlated with the rotation rate Ω_\perp and to a lesser extent the strain rate E . Furthermore, increasing the turbulent Péclet number increases the strength of this effect and also increases the time scale over which the mass transfer rate correlates with the rotation rate. We therefore conclude that particle rotation by turbulence acts to decrease the mass transfer rate by slip. This is consistent with Batchelor’s argument that, in the limit of high turbulent Péclet number, ‘the rotation

of the particle and the ambient fluid has the effect of suppressing the convective transport due to ... streaming motions' (Batchelor 1980). However, as we observe in figures 7(b) and 12, the net effect upon the mean and fluctuations of the mass transfer rate is small when $Sr \gg 1$.

Lawson & Ganapathisubramani (2021) showed that, for neutrally buoyant spheroids, the instantaneous mass transfer rate is most strongly correlated with the velocity field $\tilde{\mathbf{v}}$ (2.13) filtered on a finite time scale $\tau_f \sim \tau_\eta Pe^{1/3}$ due to the convection-suppression effect. To test this hypothesis for sinking particles, we introduce the filtered, Lagrangian forcing terms

$$\tilde{\mathbf{E}}(t) = \frac{1}{\tau_f} \int_{-\tau_f}^0 \mathbf{E}(t + \tau) d\tau \quad \text{and} \quad \tilde{\mathbf{v}}_0(t) = \frac{1}{\tau_f} \int_{-\tau_f}^0 \mathbf{v}_0(t + \tau) d\tau, \quad (4.6a,b)$$

which specify the filtered relative velocity field in (2.13). We note that \mathbf{v}_0 only fluctuates in the particle-aligned frame and is a constant in the laboratory frame, so fluctuations in \mathbf{v}_0 are induced by turbulent rotation of the particle. We then measure the multiple correlation coefficient

$$R^2 = \frac{r_{Sh, \tilde{E}}^2 + r_{Sh, \tilde{v}_0}^2 - 2r_{Sh, \tilde{E}} r_{Sh, \tilde{v}_0} r_{\tilde{E}, \tilde{v}_0}}{1 - r_{\tilde{E}, \tilde{v}_0}^2} \quad (4.7)$$

between the instantaneous mass transfer rate Sh and the magnitudes of the filtered strain $\tilde{E} = |\tilde{\mathbf{E}}|$ and relative slip velocity $\tilde{v}_0 = |\tilde{\mathbf{v}}_0|$ as a function of the filter time scale. In (4.7), $r_{a,b}$ are the ordinary product-moment correlation coefficients of the variables indicated in the subscripts. Essentially, this measures the extent to which the linear model $\langle Sh \rangle + a_1(\tilde{v}_0 - \langle \tilde{v}_0 \rangle) + a_2(\tilde{E} - \langle \tilde{E} \rangle)$ predicts variations in Sh due to variations in \tilde{E} and \tilde{v}_0 . The result is shown in figure 14. For $Sr = 0.10$, we observe a strong correlation $r_{Sh, \tilde{E}}$ between the filtered strain \tilde{E} and the instantaneous mass transfer rate, similar to neutrally buoyant particles. As the turbulent Péclet number is increased, the time scale τ_f which maximises the strength of this correlation also increases. The additional information from \tilde{v}_0 only modestly improves the ability to predict fluctuations in Sh . However, as the sinking ratio is increased, the strength of the correlation coefficient $r_{Sh, \tilde{E}}$ decreases and fluctuations in \tilde{E} become anti-correlated with Sh at $Sr = 10$, which is consistent with our observations in figure 13 that turbulent rotation suppresses convection. In contrast, a much stronger joint correlation is observed when both the filtered strain \tilde{E} and relative velocity \tilde{v}_0 are used to predict Sh . The general trend is for the peak correlation to become weaker as the sinking ratio is increased and as the turbulent Péclet number is increased. However, an exception to this trend is seen at $Sr = 10$, where the correlation strength increases with Pe .

In figure 15, we identify the time scale $\tau_d = \arg \max_{\tau_f} R$ which maximises the multiple correlation coefficient R . We interpret this time scale as the response time of the concentration boundary layer to velocity fluctuations. In figure 15(a), we observe that the response time increases with increasing Pe approximately as $Pe^{1/3}$ and decreases with increasing Sr . This scaling is confirmed in figure 15(b), where we observe that the data collapse well when τ_d is normalised by $\tau_\eta Pe^{1/3}$. Therefore, our data are consistent with Batchelor's prediction of the convection-suppression effect in turbulent flows, provided that the time scale for averaging the relative velocity field is chosen in proportion to $\tau_\eta Pe^{1/3}$

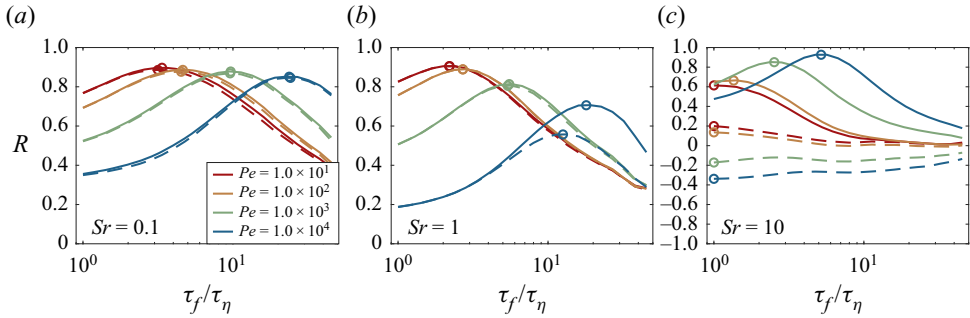


Figure 14. Joint cross-correlation coefficient of the filtered velocity field with the instantaneous transfer rate at sinking ratios of (a) $Sr = 0.1$, (b) $Sr = 1$ and (c) $Sr = 10$. The solid lines show the multiple correlation coefficient R (4.7) for varying filter time scale τ_f . The dashed lines show the ordinary correlation coefficient $r_{Sh, \tilde{E}}$ between the instantaneous transfer rate and the filtered strain magnitude \tilde{E} .

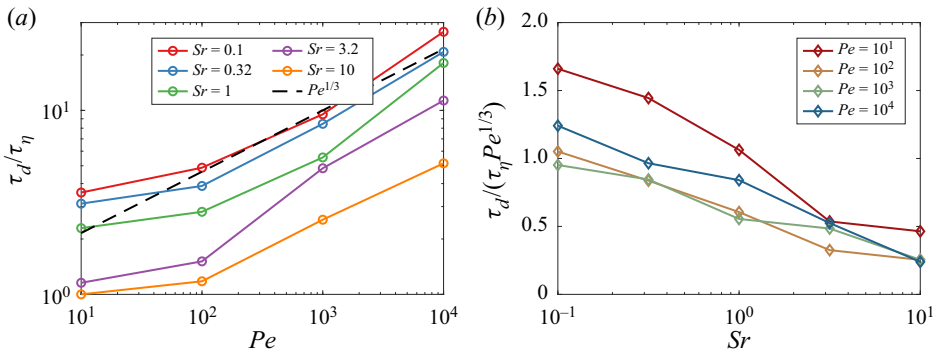


Figure 15. Identification of the response time scale τ_d of the concentration boundary layer to the fluctuating velocity field. (a) Response time scale τ_d shown as a function of Pe for varying Sr . The black dashed line shows the scaling $\tau_d \sim Pe^{1/3}$. (b) Response time scale τ_d shown as a function of sinking ratio Sr , compensated for the expected $\tau_d \sim Pe^{1/3}$ scaling.

5. Conclusion

We have examined the mechanism of mass transfer from a dilute suspension of small, sinking spheres using laboratory experiments and numerical simulations. Our starting point is to revisit the theoretical treatment by Batchelor (1980) in the small-particle limit with large but finite turbulent Péclet number. The problem is characterised by the turbulent Péclet number Pe and the sinking ratio Sr , which describes the relative magnitude of the sinking speed to the shear velocity at the particle scale. This analysis predicts a shift in the qualitative nature of the wake topology between strain-dominated flow $Sr \ll 1$, where small particles exhibit a symmetric line- or sheet-like wake structure, and slip-dominated flow $Sr \gg 1$, where solute streams along a single wake.

To validate this prediction experimentally, we conducted laboratory flow visualisation experiments which measured the local release of dye from spherical ion-exchange resin beads using a combined particle tracking and PLIF imaging technique. We are therefore able to reconstruct the instantaneous, 3-D concentration of dye released by spherical particles sinking in highly turbulent flows across a range of particle sizes and turbulence intensity, for particle Reynolds numbers within and beyond the Stokes regime ($0.11 \leq Re_w \leq 4.1$). Instantaneously and on average, when $Sr \gg 1$, we observe that dye is released

in a single wake aligned with the direction of sinking, consistent with slip-dominated mass transfer driven by sinking. However, when the sinking ratio $Sr \ll 1$, we observe instantaneous examples of dye released in sheet-like or line-like topologies, consistent with strain-dominated mass transfer driven by turbulence. On average, we observe an increasingly symmetric concentration wake as the sinking ratio is made very small. Furthermore, the average scalar field surrounding the particle is isotropised when the strength of the turbulence becomes comparable to the rate of sinking ($Sr = O(1)$). These flow visualisations qualitatively confirm a transition in the mechanism of mass transfer as the sinking ratio is varied.

To quantify this transition in mass transfer mechanism, we conducted numerical simulations of the mass transfer to small, sinking particles in the Stokes regime based on the methodology of Lawson & Ganapathisubramani (2021). The average mass transfer rate predicted by the simulations is validated against data for small particles in turbulence with $Sr \ll 1$ and is shown to approach the known asymptotic expression (4.2) for a spherical particle in uniform Stokes flow when $Sr \gg 1$. We quantify this transition in transfer mechanism using a decomposition of convective fluxes of solute away from the particle. When $Sr = 0.1$, almost all mass transfer is provided by turbulent strain, whereas at $Sr = 10$, almost all mass transfer occurs due to slip. At $Sr = 1$ the contributions are approximately equal. Cross-correlations between the mass transfer rate and convective forcing evidence the suppression of convective mass transfer by unsteady fluctuations due to the finite response time of the concentration boundary layer. For strain-dominated flow, this effect is benign: the transfer rate simply becomes responsive to strain fluctuations on longer time scales. For slip-dominated flow, we find that particle rotation by turbulence suppresses convection and the strength of the effect increases with increasing turbulent Péclet number. Therefore, our results support Batchelor's prediction that the 'strange consequence' of gentle stirring is to initially suppress mass transfer in the limit of very large Pe . However, the size of the effect is modest even at $Pe = 10^4$ and this effect may not be important in practice.

Our results have important implications for the prediction of solid–fluid mass transfer. We have seen that the sinking ratio Sr defines the mass transfer mechanism and therefore whether the dissipation rate or the slip velocity predominantly controls the mass transfer rate. This should be an important consideration in the scale-up of, for example, stirred tank reactors, where the particle size and settling velocity are often fixed, but the turbulent dissipation rate varies upon scale-up. The concept of an effective slip velocity for almost neutrally buoyant particles should also not be interpreted physically, because strain provides the mechanism of mass transfer in this scenario. Moreover, in an inhomogeneous turbulent flow, the local mechanism of mass transfer may depend upon the distribution of the kinetic energy dissipation rate. Our cross-correlation analysis has revealed that particle-scale knowledge of both the recent strain and velocity history is required to predict the instantaneous mass transfer rate. Furthermore, between the two limiting regimes at $Sr = O(1)$, both mechanisms provide comparable contributions to the mass transfer. This emphasises the need for particle-scale models which incorporate the local flow conditions. In future work, we hope to model this process using the quasi-steady approximation of Lawson & Ganapathisubramani (2021), which could be solved for an arbitrary strain–slip combination using the technique outlined in Lawson (2021).

Supplementary movies. Supplementary movies are available at <https://doi.org/10.1017/jfm.2022.998>.

Acknowledgements. The authors acknowledge the use of the IRIDIS High Performance Computing Facility, and associated support services at the University of Southampton, in the completion of this work. Pertinent data for this paper are available at <https://doi.org/10.5258/SOTON/D2455>.

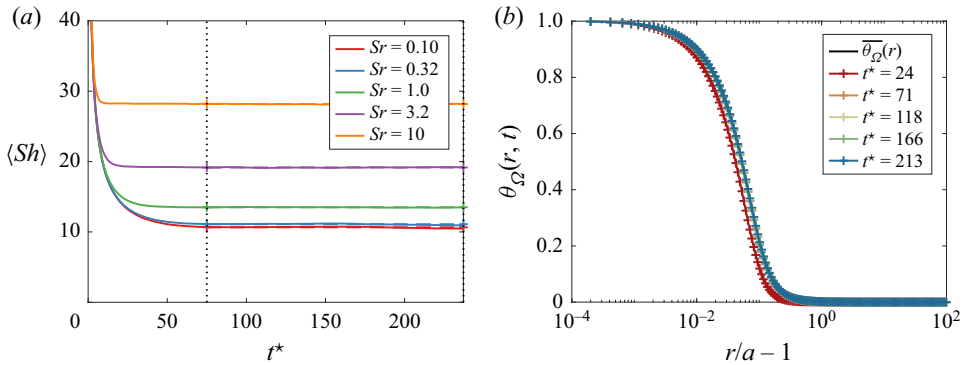


Figure 16. The approach to a statistically stationary state. (a) Evolution of the ensemble-average Sherwood number as a function of time t^* at $Pe = 10^4$ and $a/\eta = 10^{-2}$ for varying sinking velocities Sr . (b) Evolution of the shell-average concentration profile $\theta_\Omega(r, t)$ as a function of time, for the case with the longest initial transient ($Sr = 0.10, Pe = 10^4$).

Funding. This project has received funding from the European Union’s Horizon 2020 research and innovation programme under Marie Skłodowska-Curie grant agreement no. 846648.

Declaration of interests. The authors report no conflict of interest.

Author ORCIDs.

John M. Lawson <https://orcid.org/0000-0003-3260-3538>;

Bharathram Ganapathisubramani <https://orcid.org/0000-0001-9817-0486>.

Appendix. Approach to stationary state

In this appendix, we identify the time required for our numerical simulations to reach a statistically steady state. Figure 16(a) shows an example of the initial transient in the ensemble average mass transfer rate $\langle Sh \rangle$ for different sinking rates at $Pe_\epsilon = 10^4$ and $a/\eta = 10^{-2}$, which corresponds to the longest initial transient. The transient is decreased by increasing the sinking rate and a statistically stationary state is reached after $t^* > 75$. The radially averaged concentration profile $\theta_\Omega(r, t)$ is shown in figure 16(b) for the case with the longest transient ($Sr = 0.1, Pe = 10^4$). For this extreme case, we observe the mean concentration profile has also reached its equilibrium value by $t^* = 75$.

REFERENCES

- ACRIVOS, A. & GODDARD, J.D. 1965 Asymptotic expansions for laminar forced-convection heat and mass transfer. Part 1. Low speed flows. *J. Fluid Mech.* **23** (1965), 273–291.
- ALCOLOMBRI, U., PEAUDECERF, F.J., FERNANDEZ, V.I., BEHRENDT, L., LEE, K.S. & STOCKER, R. 2021 Sinking enhances the degradation of organic particles by marine bacteria. *Nat. Geosci.* **14** (10), 775–780.
- ARMENANTE, P.M. 1983 Mass transfer to microparticles in agitated systems. PhD thesis, University of Virginia.
- ARMENANTE, P.M. & KIRWAN, D.J. 1989 Mass transfer to microparticles in agitated systems. *Chem. Engng Sci.* **44** (12), 2781–2796.
- BATCHELOR, G.K. 1979 Mass transfer from a particle suspended in fluid with a steady linear ambient velocity distribution. *J. Fluid Mech.* **95**, 369–400.
- BATCHELOR, G.K. 1980 Mass transfer from small particles suspended in turbulent fluid. *J. Fluid Mech.* **98** (3), 609–623.
- BELLANI, G. & VARIANO, E.A. 2014 Homogeneity and isotropy in a laboratory turbulent flow. *Exp. Fluids* **55** (1), 1646.

Mechanisms of mass transfer to spheres sinking in turbulence

- CALDERBANK, P.H. & MOO-YOUNG, M.B. 1961 The continuous phase heat and mass-transfer properties of dispersions. *Chem. Engng Sci.* **16**, 39–54.
- CARTER, D., PETERSEN, A., AMILLI, O. & COLETTI, F. 2016 Generating and controlling homogeneous air turbulence using random jet arrays. *Exp. Fluids* **57** (12), 1–15.
- CLIFT, M., GRACE, J.R. & WEBER, M.E. 1978 *Bubbles, Drops and Particles*. Academic Press.
- CROWE, C.T., SCHWARZKOPF, J.D., SOMMERFELD, M. & TSUJI, Y. 2012 *Multiphase Flows with Droplets and Particles*. CRC Press.
- DE JONG, J., CAO, L., WOODWARD, S.H., SALAZAR, J.P.L.C., COLLINS, L.R. & MENG, H. 2009 Dissipation rate estimation from PIV in zero-mean isotropic turbulence. *Exp. Fluids* **46** (3), 499–515.
- DEEN, N.G., PETERS, E.A.J.F., PADDING, J.T. & KUIPERS, J.A.M. 2014 Review of direct numerical simulation of fluid-particle mass, momentum and heat transfer in dense gas-solid flows. *Chem. Engng Sci.* **116**, 710–724.
- ESTEBAN, L.B., SHRIMPTON, J.S. & GANAPATHISUBRAMANI, B. 2019 Laboratory experiments on the temporal decay of homogeneous anisotropic turbulence. *J. Fluid Mech.* **862**, 99–127.
- FENG, Z.G. & MICHAELIDES, E.E. 2009 Heat transfer in particulate flows with direct numerical simulation (DNS). *Intl J. Heat Mass Transfer* **52** (3–4), 777–786.
- FERRY, J. & BALACHANDAR, S. 2001 A fast Eulerian method for disperse two-phase flow. *Intl J. Multiphase Flow* **27** (7), 1199–1226.
- FÖRSSLING, N. 1938 Über die verdunstung fallender tropfen. *Gerlands Beiträge zur Geophysik* **52** (1), 170–216.
- GUASTO, J.S., RUSCONI, R. & STOCKER, R. 2012 Fluid mechanics of planktonic microorganisms. *Annu. Rev. Fluid Mech.* **44** (1), 373–400.
- HARRIOTT, P. 1962 Mass transfer to particles. Part I. *AICHE J.* **8** (1), 93–101.
- HIGBIE, R. 1935 The rate of absorption of a pure gas into a still liquid during short periods of exposure. *Trans. Am. Inst. Chem. Engrs* **31**, 365–389.
- JEFFERY, G.B. 1922 The motion of ellipsoidal particles immersed in a viscous fluid. *Proc. R. Soc. A* **102** (715), 161–179.
- KARP-BOSS, L., BOSS, E. & JUMARS, P.A. 1996 Nutrient fluxes to planktonic osmotrophs in the presence of fluid motion. *Oceanogr. Mar. Biol.* **34**, 71–107.
- KIM, S. & KARRILA, S.J. 1991 *Microhydrodynamics*. Elsevier.
- LAWSON, J.M. 2021 Mass transfer to freely suspended particles at high Péclet number. *J. Fluid Mech.* **913**, A32.
- LAWSON, J.M., BODENSCHATZ, E., LALESCU, C.C. & WILCZEK, M. 2018 Bias in particle tracking acceleration measurement. *Exp. Fluids* **59** (11), 172.
- LAWSON, J.M. & GANAPATHISUBRAMANI, B. 2021 Mass transfer from small spheroids suspended in a turbulent fluid. *J. Fluid Mech.* **929**, A19.
- LAWSON, J.M. & GANAPATHISUBRAMANI, B. 2022 Unsteady forcing of turbulence by a randomly actuated impeller array. *Exp. Fluids* **63** (1), 13.
- LEAL, L.G. 2012 Convection effects in low-Reynolds-number flows. In *Advanced Transport Phenomena*, vol. 135, 593–696. Cambridge University Press.
- LEVINS, D.M. & GLASTONBURY, J.R. 1972a Application of Kolmogoroff's theory to particle-liquid mass transfer in agitated vessels. *Chem. Engng Sci.* **27** (3), 537–543.
- LEVINS, D.M. & GLASTONBURY, K.R. 1972b Particle-liquid hydrodynamics and mass transfer in a stirred vessel. Part II. Mass transfer. *Trans. Inst. Chem. Engrs* **50**, 132–146.
- LI, Y., PERLMAN, E., WAN, M., YANG, Y., MENEVEAU, C., BURNS, R., CHEN, S., SZALAY, A. & EYINK, G. 2008 A public turbulence database cluster and applications to study Lagrangian evolution of velocity increments in turbulence. *J. Turbul.* **9** (31), 1–29.
- LIDE, D.R. 2013 *CRC Handbook of Chemistry and Physics, 94th Edition, 2013–2014*, vol. 53. CRC Press.
- MYERSON, A. 2002 *Handbook of Industrial Crystallization*. Butterworth-Heinemann.
- NIENOW, A.W. 1992 *The Mixer as a Reactor: Liquid/solid Systems*. Reed Educational and Professional Publishing.
- NIENOW, A.W. 2006 Reactor engineering in large scale animal cell culture. *Cytotechnology* **50** (1–3), 9–33.
- OHASHI, H., SUGAWARA, T. & KIKUCHI, K.-I. 1981 Mass transfer between particles and liquid in solid-liquid two-phase upflow in the low-velocity region through vertical tubes. *J. Chem. Engng Japan* **14** (6), 489–491.
- OUELLETTE, N.T., XU, H. & BODENSCHATZ, E. 2006 A quantitative study of three-dimensional Lagrangian particle tracking algorithms. *Exp. Fluids* **40** (2), 301–313.
- PANGARKAR, V.G. 2015 *Design of Multiphase Reactors*. John Wiley & Sons.

- PANGARKAR, V.G., YAWALKAR, A.A., SHARMA, M.M. & BEENACKERS, A.A.C.M. 2002 Particle-liquid mass transfer coefficient in two-/three-phase stirred tank reactors. *Ind. Engng Chem. Res.* **41** (17), 4141–4167.
- PÉREZ-ALVARADO, A., MYDLARSKI, L. & GASKIN, S. 2016 Effect of the driving algorithm on the turbulence generated by a random jet array. *Exp. Fluids* **57** (2), 1–15.
- RANZ, W.E. & MARSHALL, W.R. 1952 Evaporation from drops, part 1. *Chem. Eng. Prog.* **48** (3), 141–146.
- SEIDENSTICKER, S., ZARFL, C., CIRPKA, O.A., FELLEBERG, G. & GRATHWOHL, P. 2017 Shift in mass transfer of wastewater contaminants from microplastics in the presence of dissolved substances. *Environ. Sci. Technol.* **51** (21), 12254–12263.
- VARIANO, E.A. & COWEN, E.A. 2008 A random-jet-stirred turbulence tank. *J. Fluid Mech.* **604**, 1–32.
- VOTH, G.A., LA PORTA, A., CRAWFORD, A.M., ALEXANDER, J. & BODENSCHATZ, E. 2002 Measurement of particle accelerations in fully developed turbulence. *J. Fluid Mech.* **469**, 121–160.
- ZEFF, B.W., LANTERMAN, D.D., MCALLISTER, R., ROY, R., KOSTELICH, E.J. & LATHROP, D.P. 2003 Measuring intense rotation and dissipation in turbulent flows. *Nature* **421** (6919), 146–149.